

Hydrodynamics of Micropipette Aspiration

Jeanie L. Drury and Micah Dembo

Department of Biomedical Engineering, Boston University, Boston, MA 02215 USA

ABSTRACT The dynamics of human neutrophils during micropipette aspiration are frequently analyzed by approximating these cells as simple slippery droplets of viscous fluid. Here, we present computations that reveal the detailed predictions of the simplest and most idealized case of such a scheme; namely, the case where the fluid of the droplet is homogeneous and Newtonian, and the surface tension of the droplet is constant. We have investigated the behavior of this model as a function of surface tension, droplet radius, viscosity, aspiration pressure, and pipette radius. In addition, we have tabulated a dimensionless factor, M , which can be utilized to calculate the apparent viscosity of the slippery droplet. Computations were carried out using a low Reynolds number hydrodynamics transport code based on the finite-element method. Although idealized and simplistic, we find that the slippery droplet model predicts many observed features of neutrophil aspiration. However, there are certain features that are not observed in neutrophils. In particular, the model predicts dilation of the membrane past the point of being continuous, as well as a reentrant jet at high aspiration pressures.

INTRODUCTION

The diameter of a neutrophil is on the order of twice the diameter of a typical capillary vessel ($9\ \mu\text{m}$ versus $4.5\ \mu\text{m}$) (Ting-Beall et al., 1993). These cells are therefore forced to repeatedly undergo cycles of large deformation and recovery as they pass through the systemic and pulmonary circulations. The rheological behavior of a cell as it undergoes these deformations is passive (i.e., the necessary energy is supplied by the transcapillary gradient of blood pressure, which in turn is generated by the action of the heart). In addition, there is considerable circumstantial evidence indicating that the blockages caused by white cells stuck inside capillaries can contribute to pathology during acute ischemic incidents (Sutton and Schmid-Schönbein, 1992). Thus, despite the low numbers of white blood cells, the incidence of heart attack is directly correlated with the white cell count (Friedman et al., 1974; Prentice et al., 1982; Schmid-Schönbein and Engler, 1986).

Experimental studies of the physiological process by which white cells pass into and out of small capillaries have frequently been based on cell behavior during micropipette aspiration and on the subsequent recovery of the cells to their resting spherical shape. The general and rather remarkable conclusion of such work is that circulating granulocytes are rather like droplets of liquid mercury (i.e., they are incompressible Newtonian fluids, they are very slippery, and they have a considerable surface tension) (Evans and Kukan, 1984).

Although few dispute the fact that this simple model is remarkably close to the truth, there remains plenty of room in which to quibble about details. For example, Evans and Yeung have presented a model in which the surface layer of

the granulocyte is characterized by a surface shear and dilatation viscosity in addition to a constant cortical tension (Evans and Yeung, 1989; Yeung and Evans, 1989). Other groups have presented calculations in which the interior of the leukocyte is modeled as a standard viscoelastic solid (Schmid-Schönbein et al., 1981) or as a Maxwell fluid inside a prestressed elastic cortical shell (Dong et al., 1988, 1991; Dong and Skalak, 1992). More recently it has been postulated that the neutrophil behaves as a pseudoplastic or power law fluid (Tsai et al., 1993). In related developments it has been suggested that the apparent surface tension of the white cell should not be treated as a constant, but instead should be regarded as a function of surface dilation (Needham and Hochmuth, 1992). Finally, it has been put forth that at very high rates of aspiration, friction in the lubrication layer between the cell and the capillary wall can have a significant effect (Shao and Hochmuth, 1997).

One may thus stipulate that all of the simple features of the slippery droplet model have been questioned at one time or another. Nevertheless, a decision as to whether one or another of the suggested improvements to the slippery droplet model is actually justified requires accurate numerical studies for each case and comparison of such studies with experiments. Before undertaking such testing, however, it seems that one would be well advised to first understand the pluses and minuses of the simplest interesting case in some detail. Therefore our objective in the current paper is mainly to present some results that will serve to indicate exactly what does and does not happen when a slippery droplet of Newtonian fluid is aspirated into a tube.

THEORY

The Stokes equations

Introducing cylindrical coordinates (r, θ, z) , we will henceforth consider a “pipette” to be a cylindrical cavity or tube drilled into the half-space $z > 0$. We denote the interior

Received for publication 6 July 1998 and in final form 14 September 1998.

Address reprint requests to Dr. Micah Dembo, Department of Biomedical Engineering, Boston University, 44 Cummington St., Boston, MA 02215-2407. Tel.: 617-353-1671; Fax: 617-353-6766; E-mail: mxd@bu.edu.

© 1999 by the Biophysical Society

0006-3495/99/01/110/19 \$2.00

caliber of the pipette by R_p . The two-dimensional manifolds $\{r > R_p; z = 0\}$ and $\{r = R_p; z > 0\}$ are then called the exterior and interior surfaces of the pipette, respectively (see Fig. 1). The portion of a pipette boundary that cannot be clearly classified as interior or exterior is called the “nozzle.” For purposes of our current discussion, the nozzle then consists only of the circular locus $\{r = R_p; z = 0\}$. One should bear in mind that our simplified model for a pipette neglects the fact that real pipettes have a finite “lip” characterized by a small but nonzero radius of curvature.

The particular abstractions considered by us to be representative of neutrophils will be simple droplets of an incompressible and slippery Newtonian fluid. Therefore to avoid confusion, we shall henceforth use the word “droplet” when we mean to refer to such a simplified model of a cell. We will generally assume that at an arbitrary instant of time such a droplet can be said to occupy some simply connected region, $\Omega(t)$, that this region has radial symmetry, and that its boundary is piecewise smooth. At $t = 0$, we take Ω to be a sphere of radius R_c . We also assume that this sphere touches the pipette along the ring formed by the sharp corner of the nozzle and that at all subsequent times the gasket formed by the contact of the droplet and the nozzle remains leakproof. This last assumption ensures that the

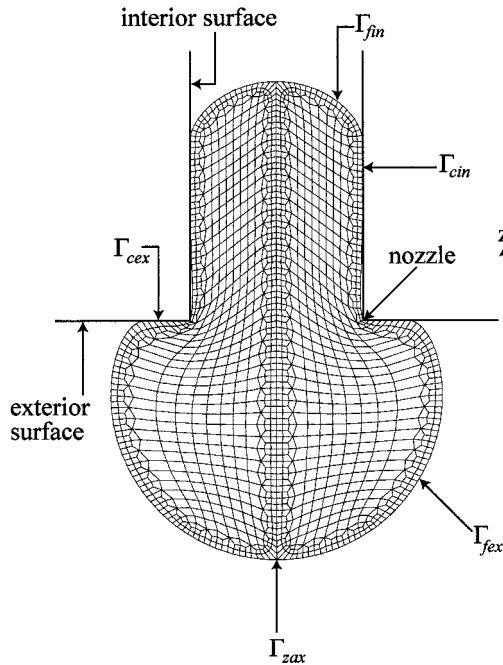


FIGURE 1 Geometry of the “pipette” and “droplet” for the conditions of the standard aspiration calculation. The “exterior,” “interior,” and “nozzle” of the pipette are indicated. The geometry of the droplet is described by an axisymmetrical domain Ω that is initially taken to be a sphere of radius R_c . We denote the interior caliber of the pipette by R_p . The various submanifolds that comprise the boundary of the pipette are indicated, where Γ_{fex} , Γ_{cex} , Γ_{fin} , Γ_{cin} , and Γ_{zax} refer to the free-exterior boundary, the constrained-exterior boundary, the free-interior boundary, the constrained-interior boundary, and the logical boundary (associated with the axis of rotation), respectively.

regions of bathing fluid inside and outside the lumen of the pipette are effectively disconnected.

The requirements of incompressibility and momentum balance within the droplet lead to the Stokes equations:

$$\nabla \cdot \mathbf{v} = 0 \quad (1a)$$

and

$$\nabla \cdot (\mu(\nabla \mathbf{v} + (\nabla \mathbf{v})^T) - p\mathbf{I}) = 0, \quad (1b)$$

where p and \mathbf{v} are the pressure and velocity fields, μ is viscosity, and \mathbf{I} is a unit tensor.

Boundary conditions

Because the pipette is solid and immovable, portions of the droplet’s boundary that contact its interior or exterior surfaces are constrained and prevented from further motion in the direction of the outward normal. On the other hand, because the droplet is assumed to be perfectly slippery, contact of the droplet with the pipette does not imply complete cessation of fluid motion (i.e., the fluid can still flow in the tangent direction).

In any event, the interaction of the droplet with the pipette means that when enforcing boundary conditions, it is generally necessary to consider the surface of a droplet as comprising the union of several submanifolds Γ_{fin} , Γ_{cin} , Γ_{cex} , and Γ_{fex} . These are the free-interior, constrained-interior, constrained-exterior, and free-exterior surfaces of the droplet, respectively (see Fig. 1). All of these manifolds can grow or shrink in extent and shape as functions of time, and in some configurations certain manifolds (e.g., Γ_{cex}) may not exist at all. There is a fifth boundary, Γ_{zax} , which exists at the axis of rotation. This is a purely logical boundary that is important numerically but which has no physical significance.

Generally we will let \mathbf{n} and \mathbf{t} denote unit normal and tangent vectors on the surface of the droplet (\mathbf{n} will point in the outward direction and \mathbf{t} in the direction of increasing latitude). We also let κ be the mean curvature of the free surface of the droplet, γ be the droplet surface tension, P_{in} be the hydrostatic pressure acting on the free surfaces of the droplet inside the lumen of the pipette, and P_{ex} be the pressure acting on the free surfaces of the droplet outside the pipette. We may then state the boundary conditions on the four segments of the droplet periphery as follows:

$$(\mu(\nabla \mathbf{v} + (\nabla \mathbf{v})^T) - p\mathbf{I}) \cdot \mathbf{n} = -(2\kappa\gamma + P_{in})\mathbf{n} \quad \text{on } \Gamma_{fin}, \quad (2a)$$

$$(\mu(\nabla \mathbf{v} + (\nabla \mathbf{v})^T) - p\mathbf{I}) \cdot \mathbf{n} = -(2\kappa\gamma + P_{ex})\mathbf{n} \quad \text{on } \Gamma_{fex}, \quad (2b)$$

$$\mathbf{t} \cdot (\mu(\nabla \mathbf{v} + (\nabla \mathbf{v})^T) - p\mathbf{I}) \cdot \mathbf{n} = 0, \quad \mathbf{v} \cdot \mathbf{n} = 0 \quad \text{on } \Gamma_{cin}, \quad (2c)$$

and

$$\mathbf{t} \cdot (\mu(\nabla \mathbf{v} + (\nabla \mathbf{v})^T) - p\mathbf{I}) \cdot \mathbf{n} = 0, \quad \mathbf{v} \cdot \mathbf{n} = 0 \quad \text{on } \Gamma_{cex}. \quad (2d)$$

Measures of aspiration

Several quantities provide observable scalar measures of the extent and progress of aspiration. The most frequently reported is the axial distance separating the nozzle and the most aspirated pole of the cell, $L_p(t)$. Another useful measure of aspiration is the volume of cytoplasm contained within the lumen of the pipette, $V_{asp}(t)$. It should be remembered that because of the curvature of the cell surface, the starting value of L_p is already positive, with value $L_p(0) = R_c - \sqrt{R_c^2 - R_p^2}$. By a standard formula of analytic geometry, the starting value of the aspirated volume is $V_{asp}(0) = (\pi/6)L_p(0)(3R_p^2 + L_p^2(0))$. The rate of droplet aspiration is expressed in terms of the time derivatives $\dot{L}_p \equiv dL_p(t)/dt$ and $\dot{Q} \equiv dV_{asp}(t)/dt$.

The shape of the external surface of the droplet is characterized in terms of the maximum over the droplet surface of the radial coordinate (denoted $R_{max}(t)$). Also useful is the minimum value of the axial coordinate ($Z_{min}(t)$). In the starting condition $R_{max}(0) = R_c$ and $Z_{min}(0) = 2R_c - L_p(0)$.

Static equilibrium

For given independent parameters and initial conditions, the ultimate fate of the droplet is determined by whether the aspiration pressure is sufficient to overcome the effects of surface tension. If this is not the case, then the droplet asymptotically approaches a condition of static mechanical equilibrium in which there is only partial aspiration. To investigate the criteria for such an outcome, we first note that when the velocity field vanishes, Eqs. 1a and 1b are satisfied if and only if the pressure field inside the droplet is a constant (henceforth denoted p_{stat}). It then follows from the boundary conditions that the curvatures of the two free surfaces of a static droplet are also constants. Accordingly on Γ_{fin} ,

$$\kappa = \text{const.} = \kappa_{fin-st} = \frac{(p_{stat} - P_{in})}{2\gamma},$$

and on Γ_{fex} ,

$$\kappa = \text{const.} = \kappa_{fex-st} = \frac{(p_{stat} - P_{ex})}{2\gamma}.$$

Subtracting one of these equations from the other leads to a form of the law of Laplace:

$$\Delta P \equiv P_{ex} - P_{in} = 2\gamma(\kappa_{fin-st} - \kappa_{fex-st}). \quad (3a)$$

Several additional remarks about this equation are worthwhile. First, because spheres are the only kinds of surfaces with constant positive curvature, both Γ_{fin} and Γ_{fex} must be spherical caps at static equilibrium. Second, curvature of a spherical cap is the inverse of the radius, and the largest spherical cap that will fit inside a pipette without touching the walls has radius R_p . Hence, after some analytic geometry we can express the static curvature of Γ_{fin} as an analytic

function of L_{p-st} :

$$\begin{aligned} \kappa_{fin-st} &= \frac{2L_{p-st}}{R_p^2 + L_{p-st}^2} && \text{if } L_{p-st} < R_p \\ &= 1/R_p && \text{if } L_{p-st} > R_p. \end{aligned} \quad (3b)$$

For Γ_{fex} , similar considerations also suffice to determine the static curvature. To start with, we can write κ_{fex-st} as the inverse of the radius of a spherical cap having base R_p and volume $(4\pi/3)R_c^3 - V_{asp-st}$. The solution to this geometry problem can be written in the form

$$\begin{aligned} \kappa_{fex-st} &= \beta(8R_c^3 - 3R_p^2L_{p-st} - L_{p-st}^3)^{-1/3} && \text{if } L_{p-st} < R_p \\ &= \beta(8R_c^3 + 2R_p^3 - 6L_{p-st}R_p^2)^{-1/3} && \text{if } L_{p-st} > R_p, \end{aligned} \quad (3c)$$

where β is a shape factor bounded in the range $[2^{2/3}, 2]$. In actuality, this shape factor depends weakly on L_{p-st} in a complicated way that cannot be written in closed form. Nevertheless, for practical purposes it is sufficient to regard β as a constant with value fixed by the first term of a Taylor's expansion about the initial state: $\beta \approx (4 + (4 + 2(R_p/R_c)^2)\sqrt{1 - (R_p/R_c)^2})^{1/3}$.

Combining Eqs. 3b and 3c, we find that the difference $\kappa_{fin-st} - \kappa_{fex-st}$ depends on L_{p-st} , R_p , and R_c only. Furthermore, if R_p and R_c are fixed, this function attains a maximum for some value of $L_{p-st} < R_p$. The precise value of L_{p-st} that yields this maximum is denoted L_{p-crit} , and the value of ΔP that causes aspiration to exactly this point is denoted by ΔP_{crit} . If we start from the standard initial conditions and apply a pressure drop $\Delta P > \Delta P_{crit}$, then Eqs. 3a, b, and c cannot be simultaneously satisfied by any choice of L_{p-st} . Thus a static equilibrium cannot exist, and the droplet will be completely aspirated. Conversely, if $\Delta P < \Delta P_{crit}$, then equilibrium will be possible for some value of $L_{p-st} \leq L_{p-crit} < R_p$.

It can be seen by direct differentiation of Eq. 3a, that in general the value of L_{p-crit} is very close to R_p . Then for a narrow pipette $R_p \ll R_c$, we can make some simplifications:

$$\begin{aligned} \Delta P_{crit} &= 2\gamma(\kappa_{fin-st}(L_{p-crit}) - \kappa_{fex-st}(L_{p-crit})) \\ &\approx 2\gamma(\kappa_{fin-st}(R_p) - \kappa_{fex-st}(R_p)) \\ &= 2\gamma(1/R_p - 1/R_c). \end{aligned} \quad (3d)$$

This formula is the basis for a simple experimental protocol for estimating the surface tension of a cell (Evans and Yeung, 1989; Zhelev et al., 1994). Using a pipette of small caliber compared to the droplet, the value of ΔP is slowly increased in small steps to the point where a further pressure step will cause continuous flow (this yields ΔP_{crit}). Finally, the surface tension is obtained according to the formula $\gamma \approx 0.5\Delta P_{crit}/(1/R_p - 1/R_c)$. In general this approach is accurate to within a few percent, even if R_p is as large as $0.5R_c$.

Dimensional analysis

Suppose that we introduce nondimensional variables: $\mathbf{t} = t\Delta P/\mu$, $\mathfrak{z} = z/R_c$, $\mathbf{r} = r/R_c$, $\mathbf{p} = (p - P_{ex})/\Delta P$, $\mathbf{v} = (\mu\mathbf{v})/(R_c\Delta P)$. After the usual algebra, it is apparent that the dimensionless version of Eqs. 1a, 1b, 2a, 2b, 2c, and 2d involves only two groups. These are the nondimensional pipette radius,

$$\mathfrak{R}_p \equiv \frac{R_p}{R_c}, \quad (4a)$$

and a form of the ‘‘capillary’’ number,

$$\mathfrak{C}_a \equiv \frac{\Delta P}{\Delta P_{crit}}. \quad (4b)$$

Other nondimensional quantities referred to in the text are as follows: $\mathcal{L}_p = L_p/R_c$, $\dot{\mathcal{L}}_p = (\mu\dot{L}_p)/(R_c\Delta P)$, $\mathfrak{R}_{max} = R_{max}/R_c$, $\mathcal{V}_{asp} = V_{asp}/R_c^3$, $\dot{\mathcal{V}} = (\mu\dot{Q})/(R_c^3\Delta P)$, and $\mathcal{A} = (\mu\dot{A})/(R_c^2\Delta P)$.

Under physiological conditions \mathfrak{R}_p usually has a value of ~ 0.5 , and in general $0 < \mathfrak{R}_p < 1$. Taking standard estimates, $\gamma \approx 3 \times 10^{-2}$ dynes/cm; $R_p \approx 3 \times 10^{-4}$ cm; and $\Delta P \approx 2 \times 10^{+4}$ dynes/cm², we find the capillary number for a neutrophil being sucked through a human capillary to be on the order of 100.

Energy conservation

If we take the dot product of the velocity field and Eq. 1b, integrate the result over the region Ω , and apply the divergence theorem, we obtain

$$0 = \int_{\Omega} 0.5\mu(\nabla\mathbf{v} + (\nabla\mathbf{v})^T) : ((\nabla\mathbf{v} + (\nabla\mathbf{v})^T) - p\mathbf{I})d\Omega - \int_{\Gamma} \mathbf{v} \cdot (\mu(\nabla\mathbf{v} + (\nabla\mathbf{v})^T) - p\mathbf{I}) \cdot \mathbf{n} d\Gamma. \quad (5a)$$

Substituting the incompressibility condition and the boundary conditions, this result can be rewritten in the form

$$\Delta P\dot{Q} = \int_{\Omega} \mu\Phi d\Omega + \gamma\dot{A}, \quad (5b)$$

where

$$\dot{Q} \equiv \int_{\Gamma_{fin} \cup \Gamma_{cin}} \mathbf{v} \cdot \mathbf{n} d\Gamma = - \int_{\Gamma_{lex} \cup \Gamma_{cex}} \mathbf{v} \cdot \mathbf{n} d\Gamma \quad (5c)$$

is the volume flux into the pipette,

$$\Phi \equiv 0.5(\nabla\mathbf{v} + (\nabla\mathbf{v})^T) : (\nabla\mathbf{v} + (\nabla\mathbf{v})^T) \quad (5d)$$

is the rate of irreversible conversion of kinetic energy to heat, and

$$\dot{A} \equiv \int_{\Gamma} 2\kappa\mathbf{v} \cdot \mathbf{n} d\Gamma \quad (5e)$$

is the rate of change of the droplet surface area.

The interpretation of the terms in Eq. 5b is straightforward; the product of ΔP and \dot{Q} on the left gives the total power being supplied by the suction pressure. The product of γ and \dot{A} is the amount of this supply expended to create new surface area. Finally, the volume integral gives the amount of power being dissipated irreversibly as heat because of the fluid viscosity. Notice that the power used to produce changes in the kinetic energy of the droplet is neglected because of the assumption of creeping flow.

Approximate rheometric theories

After some rearrangement, Eq. 5b can be recast in the form

$$\mu = \frac{\Delta P\dot{Q} - \gamma\dot{A}}{\int_{\Omega} \Phi d\Omega}. \quad (6)$$

It will be noticed that three factors in the equation, ΔP , \dot{Q} , and \dot{A} , are directly observable (at least in principle). A fourth factor (the surface tension γ) can be derived from Eq. 3d as described previously. The remaining barrier to a practical experimental method for deriving the viscosity of a very small liquid droplet consists of the unknown dissipation integral in the denominator on the right of Eq. 6. To overcome this obstacle, it is first convenient to express the dissipation integral in nondimensional terms:

$$M(\mathbf{t}, \mathfrak{C}_a, \mathfrak{R}_p) \equiv \dot{Q}^{-2}R_p^3 \int_{\Omega} \Phi d\Omega. \quad (7)$$

Because the aspirated volume is a monotonic function of time, we may with full generality also regard M as being given in terms of \mathcal{V}_{asp} , \mathfrak{C}_a , and \mathfrak{R}_p .

For practical viscosity determinations it is necessary to tabulate numerical values of the dissipation factor M or to estimate such values by some analytic theory. The simplest existing scheme of the latter type, introduced by Needham and Hochmuth (1990), assumes that dissipation occurs only in the unaspirated portion of the droplet in the region bounded by two hemispheres. The inner hemisphere is assumed to have a radius equal to the pipette radius R_p , and an outer hemisphere is assigned a radius R_{max} (this last is used simply as a convenient measure of size of the unaspirated portion of the droplet). For values of r in the interval $[R_p, R_{max}]$, Needham and Hochmuth assume the velocity field to be strictly radial, $v_r = -\dot{Q}/(2\pi r^2)$. Applying Eq. 5d, this means that $\Phi(r) = 3\dot{Q}^2/(\pi^2 r^6)$. Finally, the dissipation

integral in Eq. 6 becomes

$$\int_{\Omega} \Phi \, d\Omega \approx \frac{3\dot{Q}^2}{\pi^2} \int_{R_p}^{R_{\max}} \frac{1}{r^6} 2\pi r^2 dr = \frac{2\dot{Q}^2}{\pi} \left(\frac{1}{R_p^3} - \frac{1}{R_{\max}^3} \right). \quad (8)$$

Comparison with Eq. 7 then shows that in the case of the Needham-Hochmuth model,

$$M \approx \frac{2}{\pi} \left(1 - \frac{R_p^3}{R_{\max}^3} \right). \quad (9)$$

Because much of the dissipation is ignored in the approximations leading to Eq. 9, the final result should be regarded as a lower bound on the actual value of M . Nevertheless, Eq. 9 suggests that the function M should be largely independent of the capillary number and of time (except to the extent that these parameters influence R_p^3/R_{\max}^3). Furthermore, when the ratio R_p^3/R_{\max}^3 is much less than 1, Eq. 9 suggests that even this minor complexity is irrelevant (e.g., during the initial phases of aspiration for narrow pipettes). Thus the Needham-Hochmuth model implies that for practical purposes of measuring viscosities, one may regard M as a constant with value on the order of $2/\pi$. Yeung and Evans (1989) used a more sophisticated model (but still with a number of approximations). The final results also suggested that M should be a constant (but with a value of ~ 2 instead of $2/\pi$). We will subsequently present actual numerical computations of the factor M .

If $M(\mathcal{V}_{\text{asp}}, \mathcal{C}_a, \mathfrak{R}_p)$ has been tabulated, then combining Eqs. 6 and 7,

$$\mu = \frac{(\Delta P - \gamma \dot{A}/\dot{Q}) R_p^3}{M(\mathcal{V}_{\text{asp}}, \mathcal{C}_a, \mathfrak{R}_p) \dot{Q}}. \quad (10a)$$

Equation 10a is exact but somewhat cumbersome, if experimental data are reported in terms of L_p . In these cases it is helpful to make further approximations: $\dot{Q} \approx \pi R_p^2 \dot{L}_p$ and $\dot{A}/\dot{Q} \approx 2(1/R_p - 1/R_{\max})$. The end result (valid if $L_p > R_p$) is as follows:

$$\mu \approx \frac{\Delta P - \gamma \dot{A}/\dot{Q}}{\pi M \dot{L}_p / R_p} \quad (10b)$$

$$\approx \frac{\Delta P R_p - 2\gamma(1 - R_p/R_{\max})}{\pi M \dot{L}_p}. \quad (10c)$$

Numerical methodology

The computations underlying this study were carried out using a low Reynolds number hydrodynamics transport code based on the Galerkin finite-element method (Hughes, 1987; Fletcher, 1984). This program was developed in recent years specifically for investigating the solutions of field theoretic formulations of the cytoskeletal mechanics and chemistry of biological cells, with particular emphasis on amoeboid cells (Dembo, 1994a,b; He and Dembo, 1997).

Many of its important features are not needed to analyze the simple computation of slippery droplet aspiration that is of immediate concern, although these additional features would be needed to treat the more complex situations mentioned in the Introduction. Descriptions of the features of this code and specifics relating to its application in the present computations are given in Appendix A.

RESULTS

As discussed previously, the dynamics of aspiration of a slippery and incompressible Newtonian droplet with constant surface tension can be fully characterized by only two nondimensional groups. These are the capillary number, \mathcal{C}_a , and the dimensionless radius, \mathfrak{R}_p (see Eqs. 4a and 4b). In the current study our basic strategy for analysis of the model is to take $\mathfrak{R}_p \in \{0.3, 0.5, 0.7\}$ and $\mathcal{C}_a \in \{0.5, 0.9, 1.25, 2, 5, 10, \infty\}$ and to exhaustively examine the complete dynamics of the aspiration for all 21 combinations of $(\mathfrak{R}_p, \mathcal{C}_a)$.

Spatial dynamics of aspiration

Figs. 2 and 3 illustrate the geometrical effects of decreasing surface tension while holding all other factors constant (after scaling, decreasing surface tension corresponds to increasing capillary number). First and foremost, one should note that when the capillary number is small (Fig. 2 *a*), the droplet merely progresses through a series of quasistatic forms as the proportions of aspirated and unaspirated liquid slowly change in time. At any given instant the shape is close to the shape of minimum surface area. Thus, for example, the exterior free surface (Γ_{fex}) can be approximated by a spherical cap with a base equal to the pipette radius. A similar cap exists in the interior of the pipette (Γ_{fin}), and, depending on the amount of aspirated fluid, there can be a cylindrical segment that is in firm contact with the interior surface of the pipette (Γ_{cin}). At a low capillary number, surface tension is sufficient to balance the suction pressure, and the droplet does not make contact with the exterior surface of the pipette (i.e., Γ_{cex} is empty).

At infinite capillary number (Fig. 2 *b*) surface tension is negligible, and the droplet geometry is not influenced by a tendency toward minimal surface area. In addition, the viscous and pressure stresses acting on the exterior of the pipette are the only factors available to balance the suction pressure. Hence there is a pronounced “flattening” of the droplet against the outer wall of the pipette (i.e., Γ_{cex} is no longer empty), and the curvatures of the free surfaces (Γ_{fex} and Γ_{fin}) are the result of the flow kinematics only. Thus these curvatures are generally much smaller than would pertain at low capillary number.

An interesting feature of aspiration at low surface tension is the development of a slight cervix just interior to the pipette opening (see *inset* of Fig. 2 *b*). This leaves a gap between the droplet surface and the interior wall of the pipette. The manifold Γ_{fin} then consists of two disconnected

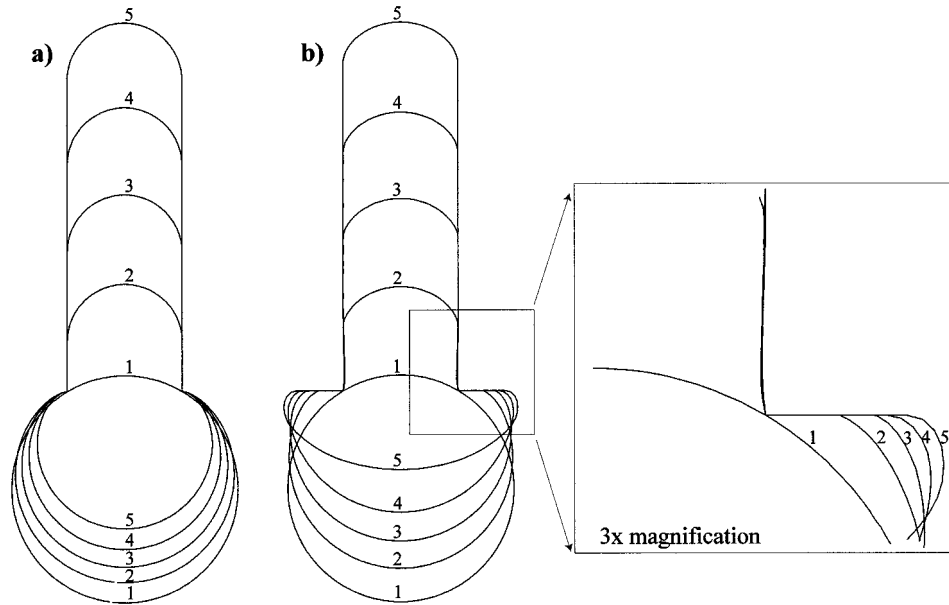


FIGURE 2 Overlay plot illustrating changes in the shape of a Newtonian droplet during aspiration as a function of capillary number. (a) $\mathcal{C}_a = 2$. (b) $\mathcal{C}_a = \infty$. For *a*, *b*, and the inset, the degree of aspiration is (1) 0%, (2) 15%, (3) 30%, (4) 45%, and (5) 60% for $\mathfrak{R}_p = 0.5$. (a) At low capillary number, aspiration of the droplet proceeds through a series of quasistatic states. The unaspirated portion of the droplet maintains the geometry of a spherical cap, whereas the aspirated portion has the geometry of a cylinder with a hemispherical cap of radius R_p . (b) At high capillary number, there is a pronounced “flattening” of the exterior portion of the droplet against the outer surfaces of the pipette. Also predicted is a decrease in the curvature of the surface Γ_{fin} . A further prediction is the existence of a small stable gap between the droplet surface and the interior wall of the pipette. This gap, as well as the “flattening,” can be further observed in the inset.

parts (the surface of the cervix and the rounded surface at the apex of the droplet). Intuitively one might expect a propensity of this cervix to deepen and pinch off in a fashion similar to what happens in a dripping faucet. Remarkably, however, we find that the saddle-like free surface of the cervix is stable regardless of pipette radius and regardless of capillary number. This stability is mediated by a precarious balance between the viscous stresses, the hydrodynamic pressure, and the negative suction pressure prevailing in the pipette lumen. The uncertain nature of the droplet stability at high capillary number would lead one to predict rupture (or at least tethering) for even a very slight leakage of the exterior ambient fluid in the lubrication space between the droplet and the pipette. It is also possible that the cervix would not develop at all if the external fluid were assigned a nonzero viscosity. Numerical calculations to test these possibilities will be the subject of a future study.

At low capillary number (Fig. 3 *a*), all regions of fluid on the exterior of the pipette move along streamlines that converge toward the pipette nozzle (for $\mathfrak{z} < 0$ the \mathbf{r} -velocity is negative and the \mathfrak{z} -velocity is positive and increasing; see Fig. 3, *c* and *e*, respectively). At the axis ($\mathbf{r} = 0$) the streamline has perfect axial orientation and does not change direction. The \mathfrak{z} -velocity on this streamline goes through a maximum just inside the pipette entrance and then decreases to an asymptotic value (for $\mathbf{r} = 0$, the apical \mathfrak{z} -velocity is $\sim 10\%$ smaller than the value at the pipette opening). The streamline passing along the wall of the pipette ($\mathbf{r} = \mathfrak{R}_p$) bends through a very sharp angle at the pipette opening and

then becomes perfectly aligned with the axis. Particles moving along this streamline have low \mathfrak{z} -velocity at the pipette entrance and then monotonically accelerate toward a maximum value as \mathfrak{z} increases. At intermediate values of \mathbf{r} the streamlines bend at the pipette opening. The angle of turning is such that they actually overshoot a perfect axial orientation by a small angle (hence the \mathbf{r} -velocity becomes positive for $\mathfrak{z} > 0$). The \mathbf{r} -velocity continues to increase and reaches a maximum a short distance inside the pipette. The \mathbf{r} -velocity then decreases asymptotically toward zero for very large values of \mathfrak{z} . Within the quasihemispherical apex of the droplet there are some additional flow disturbances due to the slow microscopic changes in the shape of the free surface as the distance from the pipette opening changes.

At high capillary number (Fig. 3 *b*) the flow follows a general pattern similar to the one described above, but there are two exceptional features. First, not all fluid particles on the exterior of the pipette fall on streamlines that eventually move into the nozzle (this is due to the “flattening” of the droplet). Second, the streamline passing closest to the interior wall of the pipette does not have perfect axial orientation after the pipette entrance. Rather, the \mathbf{r} -velocity along this streamline is negative up to the deepest point of the cervix (see Fig. 3 *d*). It then becomes positive (similar to the pattern of streamlines at intermediate values of the radius).

The main features of the pressure field for an aspirating Newtonian fluid are demonstrated by the contours of Fig. 3 *a* and *b*. These features include a ring of high pressure just exterior to the nozzle as well as a ring of very low pressure

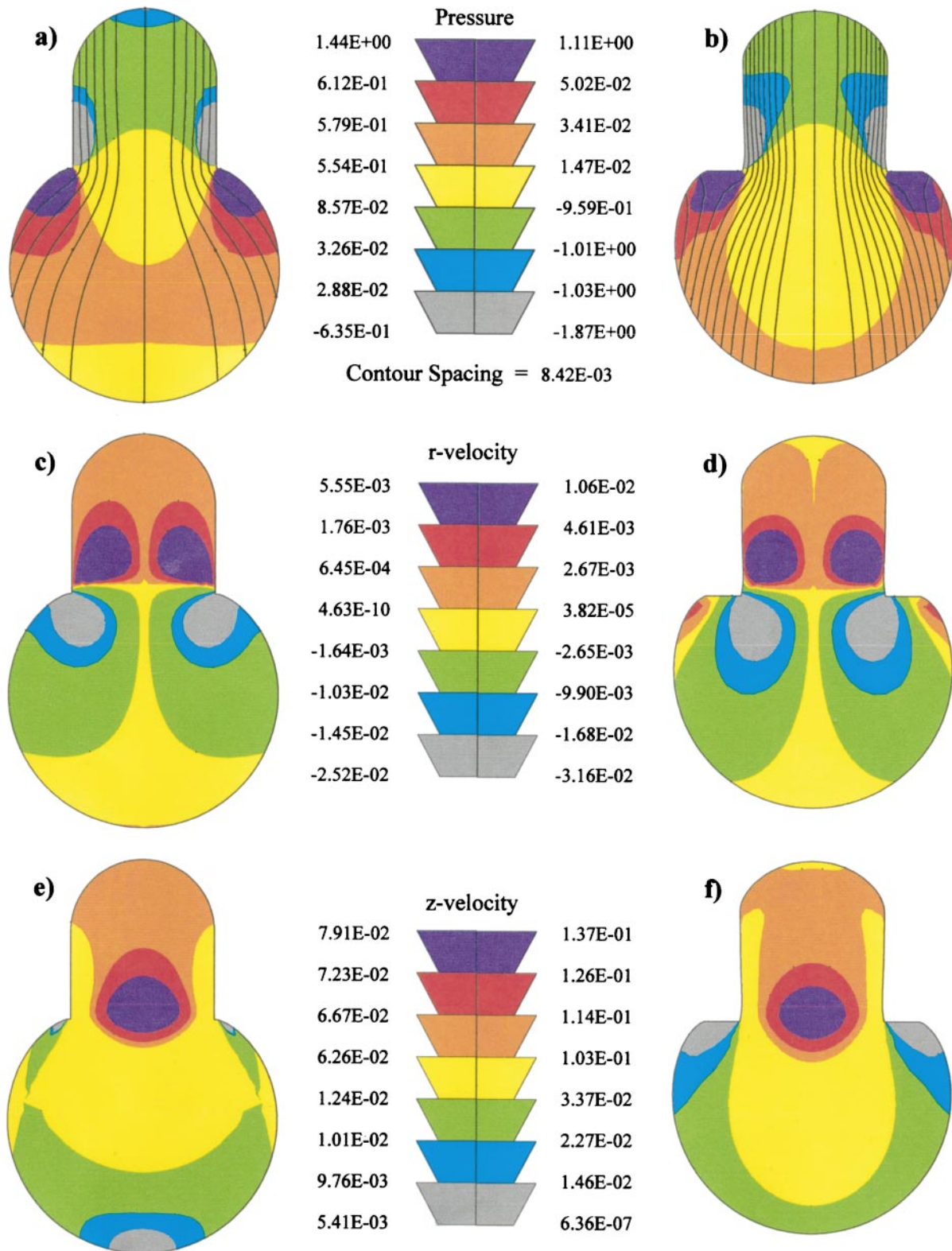


FIGURE 3 Stream functions, pressure contours, and velocity contours for $\zeta_a = 2$ (a, c, and e) and $\zeta_a = \infty$ (b, d, and f) at $\mathfrak{R}_p = 0.5$ and $\mathcal{L}_p = 1.12$. (a) Pressure contours and stream functions for $\zeta_a = 2$. (b) Pressure contours and stream functions for $\zeta_a = \infty$. (c) r-velocity contours for $\zeta_a = 2$. (d) r-velocity contours for $\zeta_a = \infty$. (e) z-velocity contours for $\zeta_a = 2$. (f) z-velocity contours for $\zeta_a = \infty$. It should be noted that in a two-dimensional view, streamlines are closer together where the highest fluid velocity occurs. In this calculation, the region of greatest volume flux is along the axis of rotation. However, as plotted, the streamlines are further apart along the axis of rotation. This distortion in the plot occurs because of radial corrections because the calculation is axisymmetrical and not two-dimensional.

just interior to the nozzle of the pipette (this is the location of the cervix in the case of high capillary numbers). The pressure gradient near the leading edge of the droplet approaches zero (as expected for simple plug flow). The pressure extremes near the nozzle and the associated radial meandering of the streamlines are both kinematically necessary for creation of the new surface area (see Appendix D for further discussion of surface kinematics during droplet aspiration).

The final stages of droplet aspiration are not particularly remarkable when the capillary number is small (Fig. 4 *a*). The shape of the droplet is still very close to the shape of minimum area, but the resistance to aspiration approaches zero because there is less and less need to deform the fluid or to produce new surface area. This leads to a singularity in the velocity of aspiration. In contrast, when the capillary number is very large, the final stage of aspiration is char-

acterized by an invagination of Γ_{fex} at the axis (called a reentrant jet). This happens because there is no penalty for the generation of surface area and because the droplet is very flattened so that a bigger pressure gradient impels the motion of fluid at the trailing pole versus the wings (something very similar happens during the final stages of the draining of a bathtub).

Fig. 4 *b* displays some stages in the formation of the reentrant jet under the condition $(\mathfrak{R}_p, \mathfrak{C}_a) = (0.5, \infty)$. In this figure, several of the previously discussed geometrical consequences of a low surface tension are evident (e.g., the development of Γ_{cex} and the cervix). An interesting observation is that Γ_{cex} continues to increase as aspiration proceeds until the beginning of the formation of the reentrant jet. Once the jet appears, Γ_{cex} decreases, but at a slow rate. A ring-like body of fluid thus becomes trapped by the exterior of the pipette as the main body of the droplet moves inward. A thin collar of fluid is all that is connecting this exterior ring with the main body of the droplet. Moreover, as the bulk of the droplet moves into the pipette, this collar becomes increasingly thinner. On this basis we feel confident in concluding that for the conditions of Fig. 4 *b* droplet rupture will ultimately occur. We observed similar dynamics under the condition of $(\mathfrak{R}_p, \mathfrak{C}_a) = (0.3, \infty)$. However, these were the only cases for which we observed rupture. For $(\mathfrak{R}_p, \mathfrak{C}_a) = (0.7, \infty)$ a reentrant jet formed, but we saw no evidence that growth of this jet would be sufficient to cause rupture. During all other computations (in which the capillary number was finite), no reentrant jet formed and there was no evidence of droplet rupture through this mechanism.

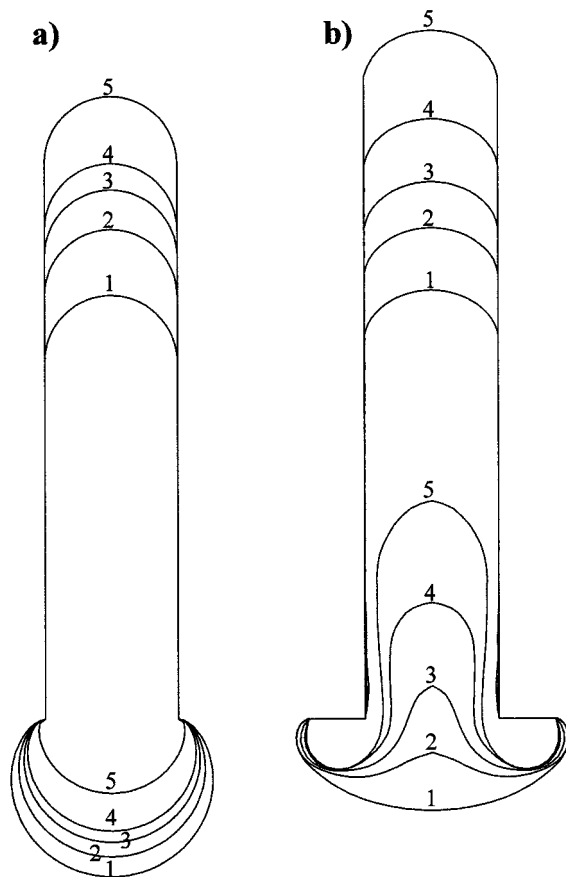


FIGURE 4 Overlay plot illustrating progressive changes in the shape of a Newtonian droplet as a function of time during the final phase of aspiration. (a) $\mathfrak{C}_a = 2$, (b) $\mathfrak{C}_a = \infty$ under the condition of $\mathfrak{R}_p = 0.5$. For *a* and *b*, the volume aspirated for each outline is as follows: (1) 60%, (2) 70%, (3) 75%, and (4) 80%. For curve *a5*, the aspirated volume is 90%, whereas the aspirated volume for *b5* is 82% because of the formation of the reentrant jet. In *a*, the final stages of aspiration, at low capillary number, progress through quasistatic equilibrium points, as was observed during the earlier stages. In *b*, however, the computation predicts the existence of a reentrant jet that grows explosively and would eventually lead to lysis in small pipettes.

Temporal dynamics of aspiration

Very commonly, the dynamics of aspiration are analyzed by plotting the length of the projection of the droplet into the pipette (\mathcal{L}_p) versus time (\mathbf{t}) (Fig. 5). In the current formulation, when the capillary number is less than 1, the pressure is not sufficient to overcome the surface tension. Thus \mathcal{L}_p increases rapidly at first but then slows down until a stable equilibrium is reached. In accord with the law of Laplace, the asymptotic value of $\mathcal{L}_p/\mathfrak{R}_p$ is less than 1 if \mathfrak{C}_a is less than 1. At capillary numbers greater than 1 the droplet moves progressively into the pipette for as long as we can follow. Thus no stable equilibrium exists. Initially the curves of \mathcal{L}_p versus \mathbf{t} are concave downward. Then when $\mathcal{L}_p/\mathfrak{R}_p$ becomes greater than 1, the curves are approximately linear. Finally, they go through a point of inflection and become concave upward. The slope of the curves then accelerates steadily.

The kinematics of aspiration are further exemplified by examining a plot of the time derivative of \mathcal{L}_p (see Fig. 6). Note that the rate of aspiration approaches a vertical asymptote as the time approaches zero, as well as at the point of complete aspiration. Between these limits there is a unique stage at which the rate of aspiration reaches its minimum

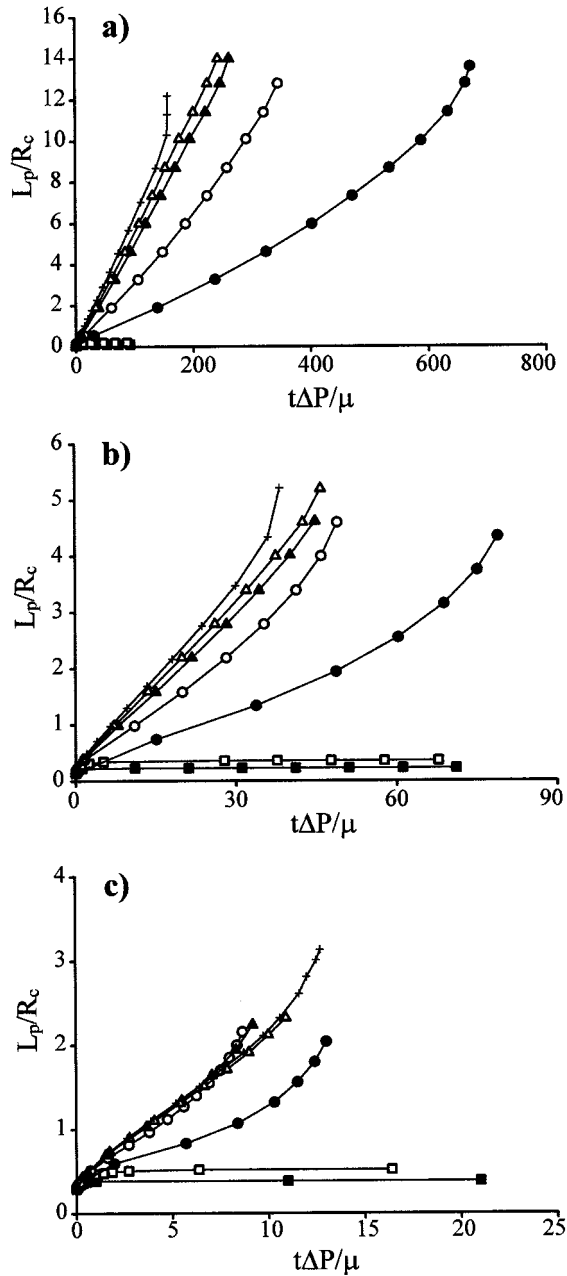


FIGURE 5 Three plots of \mathcal{L}_p versus t for (a) $\mathfrak{N}_p = 0.3$, (b) $\mathfrak{N}_p = 0.5$, and (c) $\mathfrak{N}_p = 0.7$. In *a*, *b*, and *c*, each curve represents a specific capillary number as follows: $\mathcal{C}_a = 0.5$ (■), $\mathcal{C}_a = 0.9$ (□), $\mathcal{C}_a = 1.25$ (●), $\mathcal{C}_a = 2$ (○), $\mathcal{C}_a = 5$ (▲), $\mathcal{C}_a = 10$ (△), $\mathcal{C}_a = \infty$ (+). As can be observed in *a*, *b*, and *c*, for $\mathcal{C}_a < 1$, the aspiration pressure is not great enough to overcome the surface tension, and thus aspiration stops and a stable equilibrium is reached. Furthermore, in all cases, the rate of aspiration varies with capillary number, and for the cases in *a* and *b*, the higher the capillary number, the greater the rate of aspiration. In *c*, for certain capillary numbers, the surface tension actually assists the droplet in entering the pipette by preventing excessive flattening, and thus the direct relationship of aspiration rate with pressure is not observed.

value. This minimum and the conditions associated with this minimum are important experimental observable quantities that can be used as the basis for experimental tests to distinguish between Newtonian and non-Newtonian models

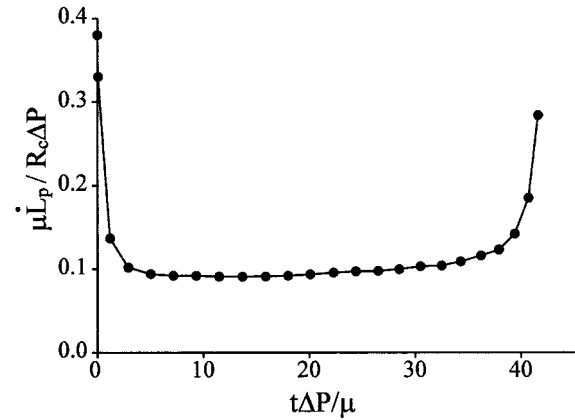


FIGURE 6 Plot of \mathcal{L}_p versus t for $\mathfrak{N}_p = 0.5$, $\mathcal{C}_a = 10$. The rate of aspiration approaches a vertical asymptote as the time approaches zero and as the point of complete aspiration is approached. Between these limits the rate of change of \mathcal{L}_p is approximately constant.

for the fluid in a microscopic droplet (this will be elaborated upon in subsequent publications).

To understand the reasons for the rapid changes in aspiration velocity during the initial stages, one must realize that the rim of the pipette is exerting a reaction force on the surface Γ_{cex} so as to exactly counterbalance the integrated suction force exerted over the manifold Γ_{fin} . The area of Γ_{cex} initially consists only of a single mesh node, and as a result the reaction force approaches that of a concentrated ring of point forces. The theoretical entry velocity for concentrated forces of this nature is infinite (sort of like entry velocity for an infinitely sharp cookie cutter pushed with a finite force). Because of the finite resolution of the computational mesh, the initial pattern of reaction forces exerted by the pipette is slightly smeared out, and thus the initial entry velocity (see Fig. 7) as computed numerically is a very slight underestimate.

For \mathfrak{N}_p equal to 0.3 and 0.5 (Fig. 5, *a* and *b*, respectively), the greater the capillary number, the greater the rate of aspiration. Intuitively this means that increasing the surface tension of the droplet always slows down droplet entry (all other factors being equal). Surprisingly, however, we find that this simple rule is not always true. In particular, it is violated when \mathfrak{N}_p is equal to 0.7 (compare the curves for $\mathcal{C}_a = 5$ (filled triangles) and 10 (open triangles) in Fig. 5 *c*). This counterintuitive result comes about because surface tension has two rather different effects on the progress of droplet aspiration. First, surface tension causes a resistance to dilation of the surface on the interior of the pipette, thus retarding entry.

The secondary effect of surface tension is more subtle and is only apparent late in the aspiration process. Here, as the exterior volume becomes smaller, the surface tension squeezes the exterior boundary, preventing distortion and flattening and providing an additional impetus for droplet entry. Simultaneously there is a decrease in viscous dissipation because the fluid in a compact rounded droplet has to

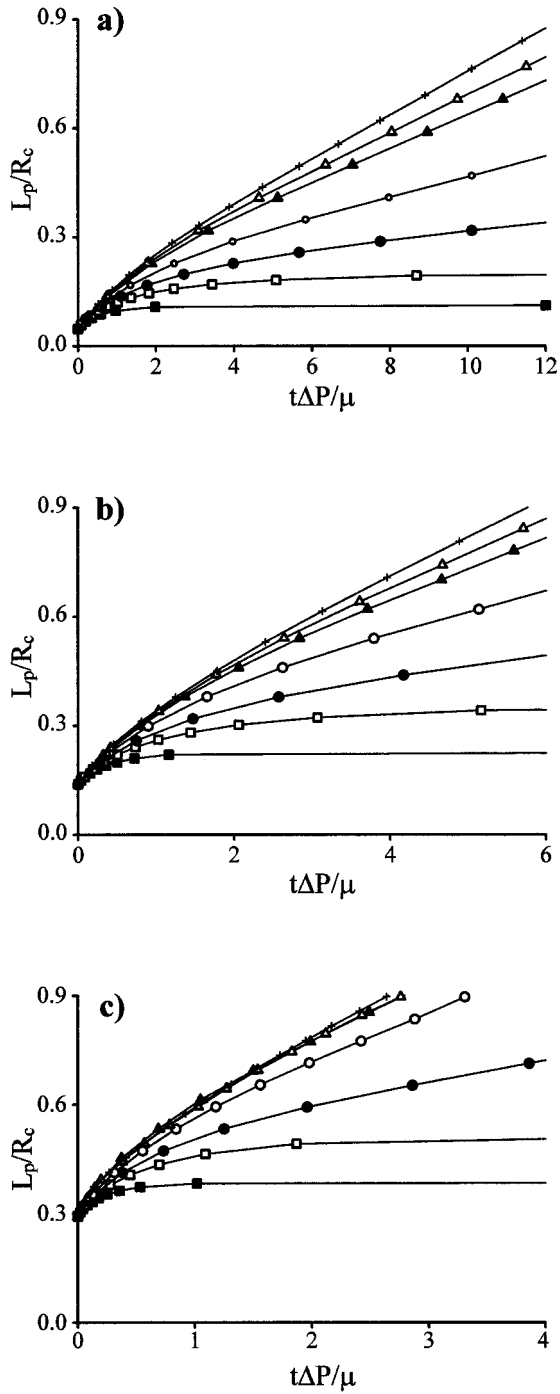


FIGURE 7 Initial entry phase for \mathcal{L}_p versus t curves for (a) $R_p/R_{\max} = 0.3$, (b) $R_p/R_{\max} = 0.5$, and (c) $R_p/R_{\max} = 0.7$. As in Fig. 5, each curve represents a specific capillary number as follows: $C_a = 0.5$ (■), $C_a = 0.9$ (□), $C_a = 1.25$ (●), $C_a = 2$ (○), $C_a = 5$ (▲), $C_a = 10$ (△), $C_a = \infty$ (+). For *a*, *b*, and *c*, the initial entry phase slope is not as steep as experiments show it to be. Rather than initially being infinite, this velocity is finite and decreasing to a constant value. The initial entry value only depends on geometry ($= \mathcal{L}_p(0)$) and is constant regardless of capillary number.

be transported over shorter distances and accelerated through smaller angles as it is aspirated. Our calculations demonstrate that on net balance, if the pipette is wide and if

the aspiration pressure is within a specific range, then these secondary kinematic benefits outweigh the primary penalty.

Calculation of viscosity

The Needham-Hochmuth (N-H) and Yeung-Evans (Y-E) models are approximate treatments of pipette hydrodynamics that have been extensively used for estimating cell viscosities from aspiration data (see Approximate Rheometric Theories; Needham and Hochmuth, 1990; Yeung and Evans, 1989). Both of these models assume that the exterior of the droplet is a spherical cap that changes only via self-similar shrinkage as its volume is aspirated. They also neglect dissipation inside the pipette and near the pipette nozzle. Using these kinematic assumptions, the models go on to derive functional relationships connecting the quantity $\mathfrak{F} \equiv (\Delta P - \gamma \dot{A}/\dot{Q})/(\mu \dot{L}_p/R_p)$ and the quantity R_p/R_{\max} . For example, in the N-H approach the result of the analysis takes the form

$$\mathfrak{F}(\Delta P, \gamma, \dot{A}, \dot{Q}, \mu, \dot{L}_p, R_p) \approx 2 \left(1 - \frac{R_p^3}{R_{\max}^3} \right). \quad (11)$$

The expression on the right of this equation is slightly different in the case of the Y-E analysis, but in either case a viscosity calculation becomes feasible because all invoked quantities except μ are experimentally observable.

Fig. 8 shows the results of a direct test for the existence of some simple formula of the sort given by Eq. 11. The open symbols give computed values of \mathfrak{F} for three different pipette radii at $C_a = 2$ (each data point corresponds to a different stage of aspiration). Similar results for aspiration at $C_a = 10$ are shown by closed symbols. The solid and dashed curves show the relevant theoretical predictions of the N-H and Y-E models, respectively.

We conclude that under many conditions there is in fact a strong semiquantitative correlation between the values of \mathfrak{F} and values of R_p/R_{\max} . It is also evident, however, that this relationship is not strictly functional (i.e., \mathfrak{F} depends on hidden factors and can undergo very significant changes without any corresponding change in R_p/R_{\max}). The hidden factors influencing \mathfrak{F} are most pronounced at high capillary numbers and at small degrees of aspiration (i.e., when the exterior shape of the droplet is nonspherical or when it is deflating in volume, primarily via processes of flattening and indentation). Even under circumstances where the exterior geometry of the droplet deflates in a similar fashion (low capillary number and intermediate levels of aspiration), both the Y-E and the N-H formulas systematically underestimate the numerically computed values of \mathfrak{F} . This, we believe, is because the underlying models do not completely account for dissipation inside the pipette and near the pipette nozzle.

To determine the viscosity of a small droplet of Newtonian fluid with improved accuracy it is desirable to use a methodology that avoids restrictive kinematic assumptions and is grounded in the concept of heat dissipation as exactly

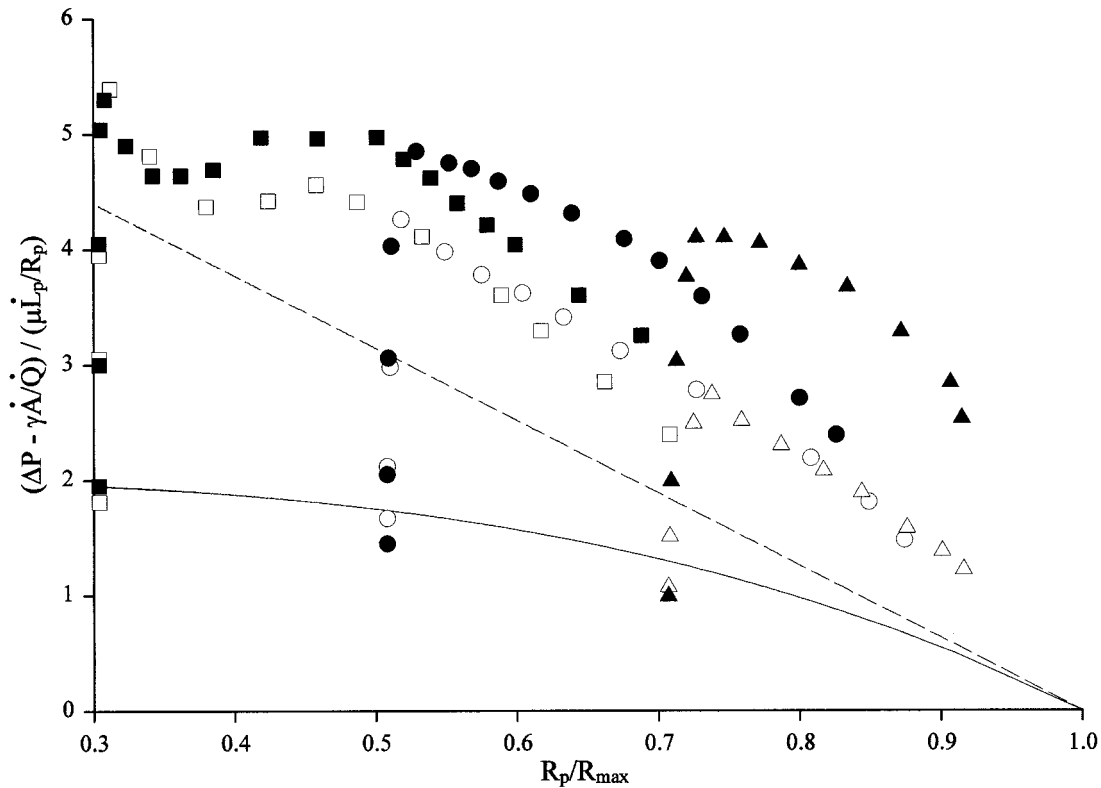


FIGURE 8 Test of the rheometric models of Needham-Hochmuth and Yeung-Evans. In this plot, the solid line represents the dissipation predicted by the Needham-Hochmuth approximation (see Eq. 11), and the dashed line represents the Yeung-Evans approximation (with $\eta = 0.01$). Data points show our computed values of the nondimensional factor, $\tilde{\delta} \equiv (\Delta P - \gamma \dot{A}/\dot{Q})/(\mu \dot{L}_p/R_p)$, at various stages of aspiration. Open symbols indicate $\mathfrak{C}_a = 2$, and closed symbols indicate $\mathfrak{C}_a = 10$. The shape of the symbol designates pipette radius (squares for $\mathfrak{R}_p = 0.3$, circles for $\mathfrak{R}_p = 0.5$, and triangles for $\mathfrak{R}_p = 0.7$). The initial vertical rise for each combination of \mathfrak{C}_a and \mathfrak{R}_p occurs because \mathfrak{R}_{max} remains essentially constant while the droplet is being indented by the pipette.

as possible. Ideally, this means use of Eq. 10a in conjunction with tables giving the dissipation factor M for relevant values of the independent variables \mathcal{L}_{asp} , \mathfrak{R}_p , and \mathfrak{C}_a . For convenience, reference tables of the necessary sort are provided in Appendix B of this paper, and a step-by-step account of a typical viscosity calculation is given in Appendix C.

The ratio \dot{A}/\dot{Q} is a measure of the production of droplet surface area per unit change in aspirated volume. This ratio appears in Eqs. 10a, 10b, and 11; and in principle, it is a function of droplet geometry and motion that should be directly observed when utilizing these equations to compute viscosities. It is particularly important to derive accurate values of \dot{A}/\dot{Q} if the capillary number is low, because this is when the corrections for surface tension are most significant. Nevertheless, because direct observations of \dot{A}/\dot{Q} are experimentally difficult, it is tempting to replace this quantity with something that is more easily determined. In the simplest such procedure (Evans and Yeung, 1989) the ratio \dot{A}/\dot{Q} is assigned a constant value based on the critical condition (i.e., $\dot{A}/\dot{Q} \approx \Delta P_{crit}/\gamma \approx 2/R_p - 2/R_c$). A more sophisticated approach is to express \dot{A}/\dot{Q} as a function of R_{max} (i.e., $\dot{A}/\dot{Q} \approx 2/R_p - 2/R_{max}$).

Fig. 9 shows a direct comparison of these formulas against our numerically computed values of \dot{A}/\dot{Q} . We con-

clude that the assumption $\dot{A}/\dot{Q} \approx \Delta P_{crit}/\gamma$ can result in large errors for all experimental conditions and should be avoided for purposes of viscosity determinations. On the other hand, for small pipette radii and at low capillary numbers ($\mathfrak{C}_a \leq 5$), the formula $\dot{A}/\dot{Q} \approx 2/R_p - 2/R_{max}$ gives very good estimates of \dot{A}/\dot{Q} , at least during the middle stages of aspiration (see Fig. 9, *a* and *b*). This covers most of the situations of interest, but one must still be careful, however, not to blithely push this approximation too far. In particular, it is not valid if $L_p \approx R_p$.

Mesh refinement

As with any computational study, one is concerned about the amount of error associated with the various necessary numerical approximations. The accuracy of the current computations has been checked by repetition at different levels of mesh refinement. Comparing plots of \mathcal{L}_p versus \mathbf{t} , we are able to detect visible differences (order of 10%) between calculations done using meshes with 272 elements versus those with 800 elements. We found virtually no difference between the results of calculations done with meshes of 800 elements versus 3200 elements (i.e., differences of less than 1%). We did observe that there was

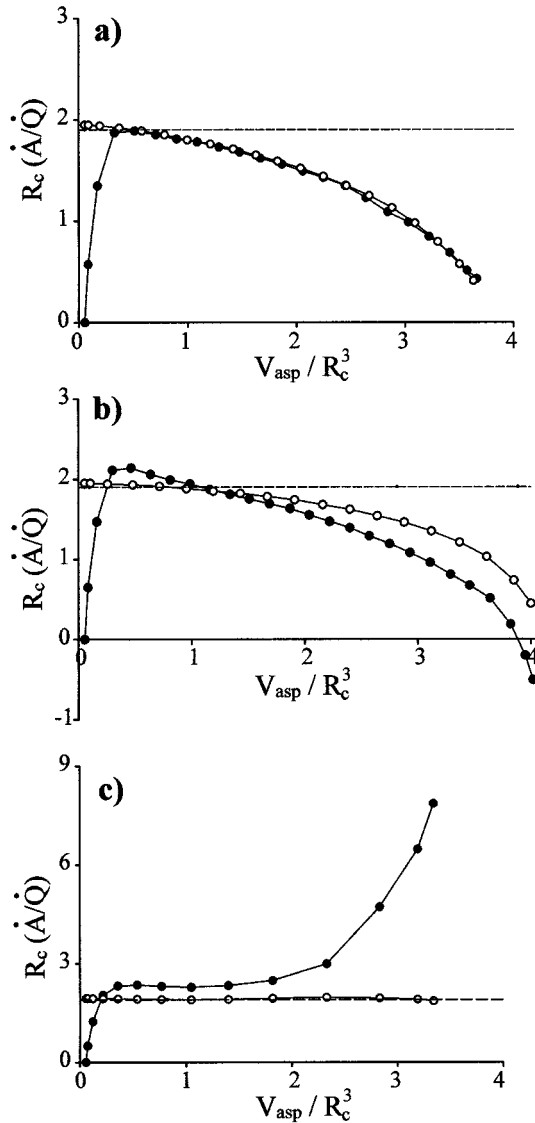


FIGURE 9 Plot of \dot{A}/\dot{Q} versus V_{asp} for both numerically calculated (\bullet) and kinematically estimated (\circ) values of \dot{A}/\dot{Q} for (a) $C_a = 2$, (b) $C_a = 10$, and (c) $C_a = \infty$. Also drawn on these plots is the line of constant \dot{A}/\dot{Q} , which is often assumed. In *a* it is evident that the kinematic model estimates the actual value of \dot{A}/\dot{Q} quite accurately, except at the very beginning of the aspiration process ($V_{asp} < V_{hemisphere}$). Also evident is the fact that \dot{A}/\dot{Q} is not a constant value. In *b* neither the assumption of constant \dot{A}/\dot{Q} nor the kinematic model is an accurate estimate for the actual value of \dot{A}/\dot{Q} . Both methods result in a gross overestimate of the actual value of \dot{A}/\dot{Q} . In *c*, however, the kinematic model and the assumption of constant \dot{A}/\dot{Q} are approximately the same and actually result in a slight underestimate of the actual value of \dot{A}/\dot{Q} , until the formation of the reentrant jet, where the numerical value of \dot{A}/\dot{Q} asymptotically approaches infinity. This result is due to the fact that the rate of volume aspiration is approaching zero.

generally a greater amount of error associated with very narrow pipettes because the deformation of the droplet is so extreme and the mesh became greatly distorted. We also found that error tended to increase as $C_a \rightarrow 1.0$. This is because the flow near the critical condition is driven on minute pressure gradients and is influenced by very small

shape changes. The latter are difficult to compute because they are superimposed on the dominant quasiequilibrium pertaining between the surface forces and the pressure field.

DISCUSSION

Although idealized and simplistic, the slippery Newtonian droplet model captures many of the features of the passive neutrophil as it is being aspirated into a micropipette. At the present time the following observations may be counted in favor of the model.

1. Under normal conditions, complete aspiration of a droplet is predicted. Thus the model is consistent with the fact that leukocytes can be aspirated at very rapid rates and at very high pressures without damage.

2. During the aspiration of passive leukocytes, there is little evidence of friction between cells and the wall of the pipette. Any sticking that does occur from time to time is probably indicative of activation. This supports the boundary conditions of the droplet model.

3. For small aspiration pressures, neutrophils behave in accordance with the law of Laplace. This means that for a given pipette radius neutrophils are characterized by a well-defined critical pressure. If the suction pressure is below this value, the cells flow inward until a static equilibrium is reached. Above the critical pressure no equilibrium exists and the cells flow completely into the pipette. Except for very narrow pipettes (less than 10% of cell radius; see below) the critical pressure depends on the cell radius and the pipette radius exactly as predicted by the law of Laplace. The static shapes of the cells after equilibration at subcritical aspiration pressures are also as predicted (i.e., curvatures of the free surfaces are constants and Eq. 3d is obeyed).

4. If the suction pressure is suddenly reduced during the middle stages of aspiration, then cells show very little tendency to recoil toward their initial rounded shape. Instead, as long as the suction pressure is still above the critical pressure, the cells continue to move inward (although the rate may be different).

5. The geometrical shapes of neutrophils during aspiration are consistent with the predictions of the droplet model. In particular, if the pressure is only slightly greater than the critical pressure, then Γ_{fex} is closely approximated by a spherical cap with a base equal to the pipette radius. Likewise, Γ_{fin} is hemispherical. There is little detectable contact with the pipette exterior. At high pressures neutrophils flatten against the exterior of the pipette, and the curvature of the interior free surface is markedly reduced (Needham and Hochmuth, 1990).

6. If the suction pressure is steady, the kinetics of neutrophil aspiration are qualitatively consistent with the predictions of the droplet model. Thus the initial rate of entry (as measured in terms of \dot{L}_p) is virtually infinite. The rate of aspiration slows down very quickly and becomes approximately constant. The phase of constant aspiration rate is prolonged and continues until the radius of the unaspirated

material approaches the pipette radius. During the final stages of aspiration L_p increases and again approaches infinity.

7. According to some experiments, the value of L_p observed during the middle range of the aspiration process is approximately linear in the suction pressure (Evans and Yeung, 1989; Needham and Hochmuth, 1990).

8. If cells are completely aspirated into a pipette, held for ~ 5 s in the final “cigar-like” shape, and then expelled, they will spontaneously regain their original spherical shape. Analysis of the rate of recovery of the original round shape is quantitatively consistent with a model in which the sole driving force comes from surface energy (Tran-Son-Tay et al., 1991). Notably the recovery kinetics are not consistent with models involving significant contributions of elastic energy. The values of surface tension and viscosity determined from aspiration experiments are portable and can quantitatively predict the kinetics of freely recovering neutrophils in these experiments.

We will now list several instances in which existing experimental observations do not favor the droplet model:

1. During the initial stages of pipette aspiration, neutrophils flow rapidly, and only after some time does the stage of slow steady aspiration begin. This is qualitatively consistent with the kinetics predicted by the droplet model, but the quantitative data are impossible to reconcile. In particular, the experimentally observed amplitude of the initial rapid entry phase at high suction pressures (several pipette diameters) is much larger than anything predicted by our calculations (see Fig. 10 for comparison of the model with experimental data).

2. There has been evidence presented indicating that L_p is highly nonlinear in the aspiration pressure (Tsai et al., 1993; Waugh and Tsai, 1994). In this case it was been suggested that the cytoplasm of the neutrophil should be represented as a power law fluid (also sometimes called a shear thinning fluid or a pseudoplastic fluid).

3. If the neutrophil is aspirated very quickly and then immediately expelled from the pipette, the recovery process begins with brief initial “jump” or recoil toward the spherical shape. If the cell is held inside the pipette for a few seconds before being expelled, then this initial transient is not observed (see item 8 above). This suggests that the neutrophil has a fading elastic memory with a time constant on the order of 1 s (Tran-Son-Tay et al., 1991).

4. When the neutrophil is aspirated into a very small pipette (less than 30% of cell radius), aspiration continues until all of the wrinkles and folds of the lipid membrane are pulled smooth. Shortly past this point lysis occurs if any further aspiration is attempted (Evans and Yeung, 1989). In the droplet model, this hard limit on the total surface dilation does not occur (see further analysis in Appendix D).

5. If a neutrophil is partially aspirated into a narrow pipette, then the cell may appear to reach a new equilibrium state even while there is still excess surface area available. If the suction pressure is then rapidly stepped to a very high level before being returned to the equilibrium level, one observes in-phase increases and decreases of L_p (Zhelev and

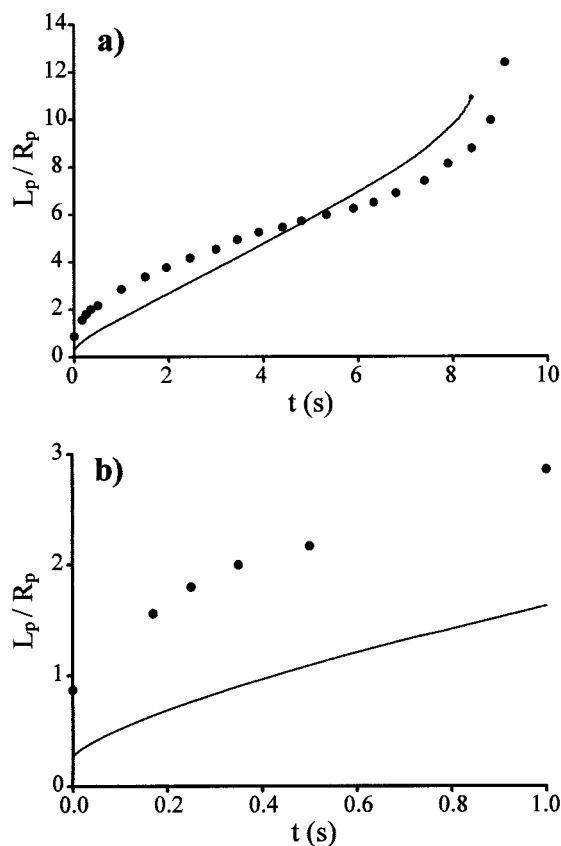


FIGURE 10 Plot of L_p/R_p versus t , comparing model predictions and data (from figure 8 of Tsai et al., 1993) for (a) complete course of aspiration and (b) initial entry phase. The viscosity was adjusted to obtain the best fit with experiment, whereas other parameters were fixed as described in the original publication: $\Delta P = 4900$ dynes/cm², $\mu = 925$ dynes \cdot s/cm², $\gamma = 0.035$ dynes/cm, $R_c = 4$ μ m, and $R_p = 2$ μ m. It is evident that the initial phase of neutrophil aspiration is faster and has a larger amplitude than one would expect for a slippery droplet.

Hochmuth, 1994). These are similar to the changes one would expect for an elastic object, and they cannot be accounted for by the droplet model. One may speculate that large changes in the material properties of the neutrophil can be induced by stretch activation of receptors on the plasma membrane.

6. Zhelev and co-workers (1994) have shown that in very small pipettes the static equilibrium of the neutrophil is not exactly described by the law of Laplace. The discrepancies can be accounted for by including a finite thickness of the cortical layer responsible for generating the apparent surface tension. Some bending rigidity of the cell surface may also be indicated.

7. For very narrow pipettes (0.4 μ m) and for very high suction pressures a necking instability is induced during aspiration experiments (Zhelev and Hochmuth, 1995). We have shown that this kind of instability is not consistent with the droplet model. It may be possible, however, to reproduce the observed behavior by allowing for flow in the small gap separating the cell and the pipette.

Clearly the droplet model has to be improved, but even in its simplest form it does provide a reliable account of the main mechanical features of the neutrophil. The two fundamental parameters of the model (i.e., the cell viscosity and the cell surface tension) are therefore of extreme interest, and many ongoing studies are aimed at elucidating the molecular basis of these coefficients.

Unfortunately, an analysis of the current literature indicates that in the case of the cytoplasmic viscosity all values now available have been derived using ad hoc and highly inaccurate procedures and assumptions. If applied to an ideal Newtonian droplet, the viscosity values obtained using these approaches would yield correct order-of-magnitude estimates, but they would be subject to systematic errors. For example, large changes in apparent viscosity could be completely caused by differences in pipette diameter, in aspiration pressure, or in surface tension. To reliably correct for such factors we would suggest use of a rheometric procedure based on Eqs. 10a, 10b, or 10c in conjunction with our numerically computed values of the dissipation factor (see Appendices B and C). This is the most utilitarian outcome of our present calculations.

Our calculations have also revealed two qualitative features of the droplet model that could serve as the basis for further experimental tests of its validity. In particular, we find that at very high suction pressures a reentrant jet should develop during the final stages of aspiration. We also find that at high capillary numbers a small stable cervix should develop just inside the pipette opening.

APPENDIX A: NUMERICAL METHODS

Data structure

Fig. 11 shows a typical finite-element mesh defining the region Ω , both in the initial condition (Fig. 11 *a*) and after some degree of aspiration (Fig. 11 *b*). Notice that the mesh interior consists of the union of nonoverlapping quadrilaterals $i_Q = 1, \dots, n_Q$, and that the mesh boundary comprises straight line segments or edges $i_L = 1, \dots, n_L$. The vertices nodes that define the corners of the quadrilaterals and/or the end points of the edges are $i_N = 1, \dots, n_N$. Each of the quadrilaterals is specified by pointers $I_{NQ} = (i_{N1}, i_{N2}, i_{N3}, i_{N4})$ that give the indices of the four vertex nodes of the quadrilateral. In a similar fashion, each of the line segments or edges of the boundary is specified by pointers $I_{NL} = (i_{N1}, i_{N2})$ that give the indices of the two vertex nodes of the edge.

The ordering of the nodes in I_{NL} is assumed to be such that an observer standing in the interior of the mesh will see the line segment from i_{N1} to i_{N2} as a step in a counterclockwise traversal of the mesh boundary. The ordering of the nodes in I_{NQ} is assumed to be such that an observer standing in the interior of the quadrilateral will see the four line segments $i_{N1} \rightarrow i_{N2}$, $i_{N2} \rightarrow i_{N3}$, $i_{N3} \rightarrow i_{N4}$, $i_{N4} \rightarrow i_{N1}$ as consecutive steps in a counterclockwise traversal of the quadrilateral boundary.

To host the dynamical equations, each of the vertex nodes is associated with a vector of quantities that defines the position of the node and, by the values of the velocity, the pressure and such other dynamical fields as may be of interest. Thus for the present computation the node vector for the node with index i_N has the structure $\mathbf{U}_{i_N} = (r, z, v_r, v_z, p, \dots)$. Each of the line segments or edges of the boundary is also characterized by a vector of dynamical variables, $\mathbf{U}_{i_L} = (\rho, \dots)$. Each line segment of the mesh boundary is further characterized by a pointer that indicates the type of the active boundary condition on this segment. Thus in the present application this boundary condition pointer could be directed toward any one of the four physical boundary types Γ_{ex} , Γ_{cex} , Γ_{fin} , or Γ_{cin} . Because we assume

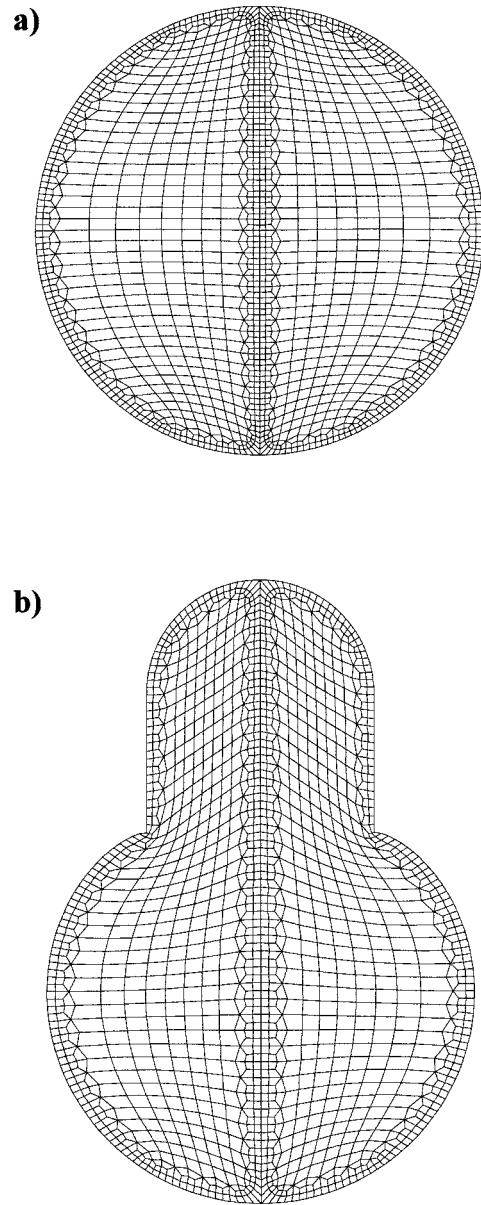


FIGURE 11 Typical mesh of quadrilateral elements used in these computations. (a) Initial round mesh with $i_N = 897$, $i_L = 192$, and $i_Q = 800$. (b) Same mesh as after partial aspiration. The mesh adapts from the round configuration to the aspirated shape strictly by changes in the placement of the vertex nodes. No changes in the connectivity on the mesh nodes are necessary. In controls to test numerical convergence (see Results) we have occasionally used a simpler mesh (272 elements) and a more complex mesh (3200 elements). Note that the computation is axisymmetrical, so that in reality the mesh encompasses only the right side of this figure. For purposes of graphical display the computational domain is redrawn in mirror reflection so as to give the final impression of what one would see in a sagittal section.

rotational symmetry, the boundary condition pointer could also be directed at a special “logical” boundary condition, Γ_{zax} , corresponding to the axis of cylindrical coordinates.

Computational cycle

The magnitude of the time step to be attempted at any point in a computation is determined by making conservative a priori estimates of the rates

at which dynamical variables are changing. In the current case the limiting factor on the time step comes from the Courant condition. (In the present study we take dt equal to the time required for the fluid to cause a displacement equal to 1% of an element diameter.) The advance of the dynamical fields over such a small time step of this magnitude is divided into individual operations, which are ultimately superimposed or assembled to obtain a final result (essentially this results in a forward Euler integration).

The splitting of operations that we employ matches most of the elementary steps with basic physical processes: chemical reaction, convective mass transport, diffusive mass transport, momentum transport, and boundary kinematics. There is also an operation that has no physical significance, namely mesh rezoning.

Interior rezoning

The paramount aim of the mesh rezone operation is to adjust the placement of the vertex nodes so as to ensure that all elements of the mesh are convex. In performing this function, physically essential attributes of the mesh must remain inviolate. This means that rezoning amounts to a constrained optimization of nodal positions in which some nodes are completely constrained (“fixed” nodes), other nodes are constrained to slide along the surface Γ (“boundary” nodes), and still other nodes are completely free.

In the current application, nodes that fall on the interface between different boundary segments are fixed as far as interior rezoning is concerned. Thus, for example, if the droplet touches the inside of the pipette, then the boundary Γ_{cin} is not empty and there will be at least one boundary node that lies at the junction of segments Γ_{fin} and Γ_{cin} . Such a node would be held stationary during interior rezoning. As another example, the node at the nozzle of the pipette is always fixed, because by definition it lies at the junction of $\Gamma_{fin} \cup \Gamma_{cin}$ and $\Gamma_{fex} \cup \Gamma_{cex}$. The nodes at the north and south poles of the cell are also examples of fixed nodes.

Nodes that lie on the mesh boundary but are otherwise undistinguished are examples of sliding nodes. The interior rezone operation repositions such nodes by sliding them back and forth so as to maintain an equal spacing. Nodes that are strictly in the interior of the mesh are examples of free nodes. The interior rezoner adjusts the placement of such nodes so as to optimize a measure of the convexity of the mesh quadrilaterals (the Winslow functional). The general theory of mesh generation and the details of the Winslow functional are reviewed in a recent textbook (Knupp and Steinberg, 1994).

Boundary rezoning

Once during each computational cycle the boundary rezoner determines the total length of the segments Γ_{fex} , Γ_{cex} , Γ_{fin} , Γ_{cin} , and Γ_{zax} , and computes the number of line elements comprising each of these segments. If a check reveals that the average length of edges in a particular segment is too large or too small, then the boundary rezoner takes further steps. First two elements of the segment with the greatest density are fused together. This creates a “ghost” element (i.e., an element with zero arc length). The ghost in the element topology is then progressively shifted clockwise or counterclockwise until it finds the largest segment on the boundary segment with the least resolution. This target segment is divided, with half of its arc length and the associated surface fields donated to revitalize the ghost. The boundary condition pointer for the ghost element is set to the same value as that of the target segment.

Diffusion and chemical reaction

The diffusion-reaction operator changes the node vectors according to what occurs if all processes except chemical reaction and diffusion are ignored during a small time interval. A diffusion constant is specified for each component of the node vector, as is a time derivative resulting from processes of chemical reaction. If these are zero at all nodes, the operation is terminated. The chemistry time step is taken using a first-order Runge-Kutta scheme, and a diffusion time step is taken using a Crank-Nicolson

procedure. Note that the diffusion-reaction operator is not used for the computation of droplet aspiration; nevertheless it is essential in most other computations and is therefore included here for completeness.

Advection of mass

The advection operator does two things. First, it decides the final mesh geometry, choosing the position of each node so as to optimally follow the evolving shape of the droplet. The operator next takes a fully Lagrangian time step of the linear convection equation, dilating and translating the mesh together with all associated physical quantities. The result is stored in temporary arrays. Last, quantities are interpolated from the temporary mesh onto the final mesh coordinates. This general approach is sometimes called the arbitrary Lagrange-Euler (ALE) procedure. In the current computation the mesh nodes on $\Gamma_{fex} \cup \Gamma_{fin}$ (inclusive of the north and south poles) are moved according to the local fluid velocity, and mesh nodes on $\Gamma_{cex} \cup \Gamma_{cin}$ are moved only according to the tangential fluid velocity. The node at the nozzle is held fixed (i.e., fully Eulerian). Nodes in the interior and on the z axis are also fully Lagrangian. Volumetric fields and surface fields (when present) are interpolated from the temporary mesh onto this final mesh, using a mass- and shape-preserving upwind scheme (Rash and Williamson, 1990).

Contact dynamics

The “contact” operator is concerned with the kinematics of changing boundary conditions as the droplet interacts with the pipette. This operator computes the position of the midpoint of all boundary elements. When an unconstrained surface element comes into contact with the wall of the pipette, the boundary condition pointer of this surface element is changed to reflect the appropriate constraint on the normal velocity.

Solution of the Stokes equations

The essential idea of our strategy is to consider the following perturbed version of the Stokes equations:

$$\nabla \cdot (\mathbf{v} - \epsilon \nabla p) = 0 \quad (\text{A1})$$

and

$$\nabla \cdot (\mu(\nabla \mathbf{v} + (\nabla \mathbf{v})^T) - p\mathbf{I}) = 0. \quad (\text{A2})$$

Notice that as the parameter $\epsilon \rightarrow 0$, these modified equation will come arbitrarily close to the true Stokes equation. This proposed perturbation, however, is of the “singular” type, because the small parameter multiplies a term that involves the highest order derivatives of the pressure. As a result of this singular nature we are free to specify a “numerical” boundary condition on the pressure. This we do in the natural way,

$$\nabla p \cdot \mathbf{n} = 0. \quad (\text{A3})$$

All of the other boundary conditions on the stresses and velocities in our perturbed version of the Stokes equations will be enforced just as in the original problem, Eqs. 2a, 2b, 2c, and 2d.

The optimal choice for ϵ will occur when the error in the velocity due to choice of nonzero ϵ (i.e., the perturbation caused by adding terms of $\mathcal{O}(\epsilon \|\nabla p\|)$) is on the same order as the mesh interpolation error of the velocity field. Clearly once this degree of accuracy has been achieved, further attempts to enforce incompressibility in a numerical calculation will be both wasteful and futile, because it is impossible to compute $\nabla \cdot \mathbf{v}$ with the requisite accuracy. Starting from this argument, some simple error estimates then suffice to demonstrate that for bilinear quadrilateral finite elements with characteristic radius h , an optimal approximation occurs if we take $\epsilon \sim h^2/\mu$. In actual practice we have found that solutions to the modified Stokes equations depend very weakly on ϵ . Thus essentially identical results are obtained for ϵ as low as $0.1h^2/\mu$ or as high as $2h^2/\mu$.

Note also that if there are substantial variations in the mesh resolution, then ϵ can be regarded as a function of position.

The great advantage of introducing Eqs. A1 and A2 lies the fact that these can be discretized via the standard Galerkin procedure, using simple continuous-pressure, continuous-velocity bilinear quadrilateral elements (i.e., four pressure nodes and four velocity nodes per element). This can be done despite the fact that such elements would violate the Babuska-Brezzi condition if applied to the exact Stokes equations. Thus, no special reduced integrations or nonconforming shape functions or penalty methods are necessary.

A final advantage is that the large linear system that results from the direct discretization of Eqs. A1 and A2 can be efficiently solved on the basis of a simple iterative method that has proved to be completely reliable (see, for example, Dembo, 1994a,b). This iteration is an adaptation of the Uzawa method (Temam, 1979).

If the pair (p, \mathbf{v}) is an existing approximation of the solution of the modified Stokes equations, then we obtain an improved approximation, denoted $(\hat{p}, \hat{\mathbf{v}})$, in three steps. Step one consists of regarding the pressure as known and obtaining the new estimate of the velocity field by solving

$$0 = \nabla \cdot (\mu(\nabla \hat{\mathbf{v}} + (\nabla \hat{\mathbf{v}})^T) - \mathbf{I}p), \quad \text{in } \Omega, \quad (\text{A4})$$

with standard boundary conditions, Eqs. 2a, 2b, 2c, and 2d.

Step two consists of regarding the velocity as known and then obtaining an improved estimate of the pressure as the solution of a elliptic boundary value problem,

$$\frac{1}{\mu} (\hat{p} - p) = \nabla \epsilon \nabla \hat{p} - \nabla \cdot \mathbf{v}. \quad (\text{A5})$$

Remember that $\epsilon = h^2/\mu$ is the perturbation parameter discussed previously and that the new pressure is required to satisfy the boundary condition given in Eq. A3.

The final step of the iterative cycle is the check for convergence. In the current calculations we have utilized the criterion

$$P_\delta \equiv \frac{\max(|\hat{p} - p|)}{(\max(\hat{p}) + \min(\hat{p}))} \leq 10^{-6}. \quad (\text{A6})$$

Tests indicate this degree of convergence to be effective yet fairly inexpensive.

TABLE B1 $\mathfrak{R}_p = 0.3$

\mathcal{V}_{asp}	$\zeta_a = 1.25$	$\zeta_a = 2$	$\zeta_a = 5$	$\zeta_a = 10$	$\zeta_a = \infty$
0.010	0.00	0.00	0.00	0.00	0.00
0.029	1.64 (4)	1.43 (6)	1.32 (6)	1.33 (8)	1.34 (9)
0.057	1.72 (7)	1.62 (7)	1.54 (6)	1.54 (5)	1.54 (5)
0.116	1.70 (7)	1.68 (5)	1.72 (5)	1.70 (5)	1.70 (4)
0.270	1.61 (2)	1.73 (1)	1.73 (1)	1.72 (1)	1.72 (1)
0.720	1.55 (2)	1.68 (1)	1.68 (1)	1.70 (1)	1.72 (1)
1.000	1.51 (2)	1.63 (1)	1.63 (1)	1.65 (1)	1.69 (1)
1.200	1.50 (3)	1.57 (3)	1.59 (1)	1.62 (1)	1.66 (1)
1.400	1.47 (3)	1.54 (4)	1.57 (1)	1.59 (1)	1.63 (1)
1.600	1.38 (4)	1.52 (4)	1.55 (1)	1.57 (1)	1.61 (1)
1.800	1.41 (1)	1.53 (3)	1.55 (1)	1.55 (1)	1.60 (1)
2.000	1.40 (2)	1.44 (3)	1.54 (1)	1.56 (1)	1.59 (2)
2.200	1.39 (3)	1.44 (2)	1.56 (1)	1.57 (1)	1.50 (9)
2.400	1.39 (3)	1.44 (2)	1.55 (1)	1.58 (1)	1.37 (16)
2.600	1.38 (2)	1.44 (3)	1.59 (1)	1.59 (1)	1.22 (27)
2.800	1.41 (3)	1.46 (3)	1.63 (1)	1.64 (1)	N/A
3.000	1.37 (3)	1.46 (3)	1.70 (1)	1.68 (1)	N/A
3.200	1.32 (2)	1.40 (4)	1.65 (1)	1.68 (1)	N/A
3.400	1.18 (2)	1.29 (4)	1.60 (2)	1.65 (1)	N/A
3.600	0.97 (5)	1.08 (6)	1.55 (7)	1.63 (1)	N/A
3.800	0.57 (39)	0.57 (17)	1.28 (7)	1.44 (2)	N/A
4.000	N/A	N/A	N/A	1.07 (4)	N/A

APPENDIX B: TABLES OF THE DISSIPATION FACTOR

Values of the nondimensional dissipation factor (see Eq. 7) for various choices of the independent parameters (\mathcal{V}_{asp} , \mathfrak{R}_p , and ζ_a) appear in Tables B1–B3. Quantities in parentheses are coefficients of variation (standard error expressed as percentage of estimated value). The dominant error in determining the M factor comes from the difficulty of taking numerical derivatives in time. Thus the errors reported for computations tabulated in this appendix are generally on the order of a few percent but are larger at the very start and end of aspiration because the time derivatives are changing rapidly. See Appendix C for a sample calculation in which these tables are used to obtain the viscosity of a neutrophil.

APPENDIX C: EXAMPLE CALCULATION

Step 1: Parameters obtained directly from experimental measurements

In this example, the following values were obtained from the literature (Figure 3 a of Needham and Hochmuth, 1990):

$$\Delta P = 10,175 \text{ dynes/cm}^2$$

$$\Delta P_{\text{crit}} = 175 \text{ dynes/cm}^2$$

$$V_{\text{cell}} = 2.77 \times 10^{-10} \text{ cm}^3$$

$$R_p = 2 \times 10^{-4} \text{ cm}$$

$$\dot{L}_p = 5 \times 10^{-4} \text{ cm/s}$$

$$L_p = 1.13 \times 10^{-3} \text{ cm}$$

Step 2: Calculation of other relevant data from information already obtained

$$R_c = \left(\frac{3V_{\text{cell}}}{4\pi} \right)^{1/3} = 4.04 \times 10^{-4} \text{ cm}$$

$$\gamma = \frac{\Delta P_{\text{crit}}}{2} \left(\frac{1}{R_p} - \frac{1}{R_c} \right) = 0.035 \text{ dynes/cm}$$

$$V_{\text{asp}} = \pi R_p^2 L_p - \frac{\pi}{3} R_p^3 = 1.34 \times 10^{-10} \text{ cm}^3$$

$$R_{\text{max}} \approx \left(\frac{3(V_{\text{cell}} - V_{\text{asp}})}{4\pi} \right)^{1/3} = 3.24 \times 10^{-4} \text{ cm}$$

Step 3: Computation of nondimensional parameters and variables from slippery droplet model

$$\mathfrak{R}_p = 0.5$$

$$\zeta_a = 59$$

$$\mathcal{V}_{\text{asp}} = \frac{V_{\text{asp}}}{R_c^3} = 2.03$$

TABLE B2 $\mathfrak{R}_p = 0.5$

\mathcal{V}_{asp}	$\zeta_a = 1.25$	$\zeta_a = 2$	$\zeta_a = 5$	$\zeta_a = 10$	$\zeta_a = \infty$
0.054	0.00	0.00	0.00	0.00	0.00
0.135	1.33 (4)	1.20 (6)	1.14 (6)	1.17 (8)	1.18 (8)
0.270	1.34 (9)	1.41 (8)	1.46 (6)	1.45 (5)	1.46 (5)
0.540	1.29 (11)	1.35 (5)	1.60 (6)	1.60 (5)	1.59 (4)
0.720	1.17 (3)	1.33 (2)	1.55 (1)	1.56 (1)	1.57 (1)
1.000	1.13 (4)	1.29 (2)	1.55 (1)	1.58 (1)	1.58 (1)
1.200	1.10 (4)	1.27 (3)	1.54 (1)	1.57 (1)	1.58 (1)
1.400	1.07 (3)	1.23 (3)	1.53 (1)	1.57 (1)	1.58 (1)
1.600	1.05 (3)	1.21 (2)	1.51 (1)	1.55 (1)	1.57 (1)
1.800	1.02 (3)	1.17 (3)	1.50 (1)	1.54 (1)	1.55 (1)
2.000	0.98 (3)	1.14 (3)	1.47 (1)	1.53 (1)	1.52 (1)
2.200	0.94 (3)	1.10 (3)	1.44 (1)	1.51 (1)	1.48 (2)
2.400	0.89 (3)	1.05 (4)	1.42 (1)	1.49 (1)	1.43 (3)
2.600	0.85 (3)	0.99 (4)	1.39 (1)	1.46 (1)	1.33 (6)
2.800	0.79 (4)	0.97 (3)	1.34 (2)	1.43 (1)	1.19 (10)
3.000	0.72 (5)	0.87 (5)	1.33 (1)	1.40 (1)	1.06 (15)
3.200	0.63 (7)	0.76 (6)	1.27 (3)	1.34 (1)	0.60 (14)
3.400	0.50 (12)	0.63 (7)	1.17 (4)	1.27 (1)	N/A
3.600	0.31 (18)	0.42 (8)	0.92 (11)	1.15 (3)	N/A
3.800	N/A	N/A	0.34 (6)	0.90 (7)	N/A
4.000	N/A	N/A	N/A	0.56 (12)	N/A

M can then be read from Appendix B, Table B2 (row: $\mathcal{V}_{asp} = 2.00$, column: $\zeta_a = \infty$):

$$M = 1.52$$

Step 4: Computation of viscosity using Eq. 10c

$$\mu = \frac{10175 * 2 \times 10^{-4} - 2 * 0.035 * [1 - 2 \times 10^{-4}/3.24 \times 10^{-4}]}{\pi * 1.52 * 5 \times 10^{-4}}$$

$$= 841 \text{ poise} = 84.1 \text{ Pa}\cdot\text{s}$$

This value of the viscosity is $\sim 40\%$ lower than the viscosity reported by Needham and Hochmuth for this particular cell. The discrepancy comes about mainly because of differences in the value of the dissipation functional.

TABLE B3 $\mathfrak{R}_p = 0.7$

\mathcal{V}_{asp}	$\zeta_a = 1.25$	$\zeta_a = 2$	$\zeta_a = 5$	$\zeta_a = 10$	$\zeta_a = \infty$
0.232	0.00	0.00	0.00	0.00	0.00
0.363	0.86 (4)	0.78 (7)	0.80 (7)	0.87 (7)	0.93 (8)
0.728	0.75 (6)	0.85 (2)	1.16 (4)	1.19 (2)	1.23 (2)
1.049	0.73 (11)	0.83 (2)	1.17 (2)	1.30 (4)	1.34 (1)
1.200	0.69 (6)	0.80 (2)	1.17 (2)	1.32 (1)	1.36 (2)
1.400	0.65 (6)	0.77 (2)	1.16 (2)	1.33 (1)	1.38 (1)
1.600	0.62 (3)	0.75 (2)	1.13 (3)	1.33 (1)	1.38 (1)
1.800	0.58 (2)	0.70 (2)	1.07 (3)	1.33 (1)	1.37 (1)
2.000	0.53 (2)	0.66 (3)	1.00 (4)	1.30 (1)	1.35 (1)
2.200	0.50 (2)	0.64 (3)	0.92 (4)	1.27 (1)	1.33 (1)
2.400	0.45 (2)	0.56 (4)	0.86 (4)	1.24 (1)	1.33 (6)
2.600	0.39 (5)	0.49 (5)	0.79 (4)	1.20 (1)	1.24 (3)
2.800	0.33 (5)	0.41 (5)	0.70 (6)	1.15 (1)	1.16 (2)
3.000	N/A	0.32 (10)	0.51 (8)	1.05 (5)	1.08 (3)
3.200	N/A	N/A	N/A	0.90 (8)	0.98 (10)
3.400	N/A	N/A	N/A	0.43 (10)	0.85 (4)
3.600	N/A	N/A	N/A	N/A	0.67 (6)

APPENDIX D: SURFACE KINEMATICS

Theory

It is evident that during aspiration, the wrinkled plasma membrane of a white cell is required to slide back and forth relative to the interior and to undergo various changes in folding. Little is known about the mechanical consequences or importance of these complicated gyrations, but at minimum it is necessary to suppose that the membrane will never, at any point, be stretched past the point of rupture. Furthermore, using very narrow micropipettes, Evans and Yeung (1989) have determined that this point occurs when the fractional surface dilation of the white cell reaches a value of 2.1 (area just before membrane rupture versus area of a smooth sphere with equal volume). This rather harsh constraint on the mechanics of real cells is quite blithely ignored by the slippery droplet model. In particular, the droplet surface is theoretically allowed to undergo any amount of area dilation or compression. Furthermore, despite such local dilations and compressions, the tension of the droplet surface will remain constant. To check the plausibility of these simplifications it is of interest, during calculations, to keep track of the dynamics of the droplet surface.

The weakest possible form of a surface constraint in cell mechanics consists of a global or overall constraint. Dynamically such a “weak” constraint corresponds to the assumption of a free-slip interaction between the plasma membrane and the cell interior. Because of the easy sliding of the membrane relative to the interior, any small local gradients in the amount of surface wrinkling can instantly be compensated by lateral sliding and redistribution of the membrane folds. Thus, to a good approximation, the wrinkles remain uniformly distributed over the cell surface, and a violation of the area constraint can occur only if and when the total surface area of the droplet exceeds 2.1 times the initial area. Such violations are trivial to check by direct inspection.

The “strong” or local form of the area constraint on cell mechanics postulates a no-slip interaction between the plasma membrane and the interior. Operationally this means that the fractional area dilation during aspiration must be less than 2.1 at every point on the surface. To check the consistency of the slippery droplet model versus this extreme requirement, it is necessary to introduce a special surface field: $\rho \equiv \text{cm}^2$ of actual membrane bilayer per cm^2 of “projected” surface area. Values of ρ much greater than 1 imply a highly wrinkled or ruffled membrane; ρ exactly equal to 1 implies a completely smooth membrane. Because lipid bilayers must maintain an approximately constant ratio of surface area to mass, values of ρ less than 1 can occur only after failure or rupture of the plasma membrane.

The measurements of Evans and Yeung (discussed above) imply that $\rho = 2.1$ in the starting condition when the cell has its spherical shape. Assuming a no-slip constraint between the membrane and the interior, the subsequent time evolution of ρ is governed by a continuity equation,

$$D_t \rho = -\rho \nabla_s \cdot \mathbf{v}, \quad (\text{D1})$$

where D_t is the substantial derivative for a Lagrangian observer moving with a point on the droplet surface, and $\nabla_s \cdot \mathbf{v}$ is the rate of surface dilation.

Results

As the calculation progresses, the excess area density becomes redistributed along the exterior of the cell, as seen in Fig. 12. In this case, segments with $\rho > 1$ (*thick solid histogram boundary*) still have some excess membrane stored in the form of wrinkles. Segments of the boundary with $\rho < 1$ (*open histogram boundary*) correspond to portions where the bilayer has been dilated past the point of rupture. It is clear from these results that the slippery droplet model is not consistent with the strong or local form of the surface area constraint. In fact (with the exception of some cases at low capillary number and with wide pipettes), the strong constraint predicts lysis at early stages of aspiration in the majority of our calculations. In all cases where lysis is predicted, the initial rupture was located just interior to the nozzle. This means that new droplet surface area is being created just

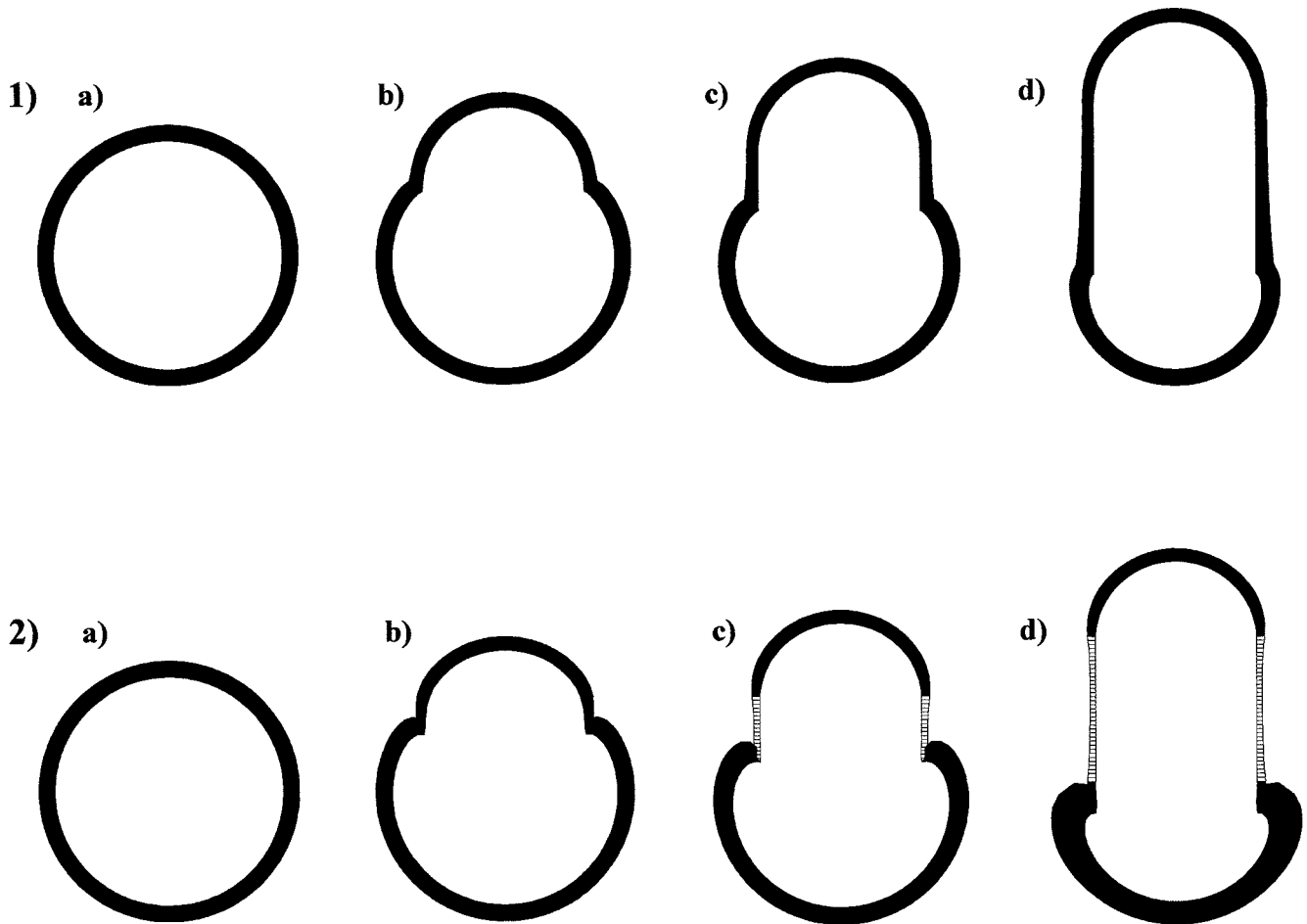


FIGURE 12 Surface density distribution. Segments with $\rho > 1$ (*thick solid histogram boundary*) still have some excess membrane stored in the form of wrinkles. Segments of the boundary with $\rho < 1$ (*open histogram boundary*) correspond to portions where the bilayer has been diluted past the point of rupture. (1 a–d) Surface density predictions for $\mathfrak{H}_p = 0.7$, $\mathfrak{C}_a = 2$, as aspiration progresses. Note that rupture of the droplet does not occur under these conditions. (2 a–d) Surface density distributions for $\mathfrak{H}_p = 0.7$, $\mathfrak{C}_a = 10$, as aspiration progresses. The portions of the boundary delimited with open histograms indicate where membrane integrity has been lost (i.e., surface dilation relative to the starting condition is greater than a factor of 2.1). In both 1 and 2, the extent of aspiration is as follows: (a) $\mathcal{L}_p = 0.29$ (initial condition), (b) $\mathcal{L}_p = 0.73$, (c) $\mathcal{L}_p = 1.21$, (d) $\mathcal{L}_p = 2.20$.

after entrance into the pipette, and this is where the ruffles of the membrane are pulled taut most rapidly.

We conclude that the plasma membrane of the neutrophil cannot be strongly coupled to the interior cytoskeleton during aspiration. On the contrary, the observed behavior of the neutrophil implies that the membrane must be able to slip easily with respect to the viscous medium in the interior. In some experiments involving aspiration at high pressure, this slippage must occur very quickly (within fractions of a second). These properties imply that the plasma membrane has little effect on the macroscopic mechanics of aspiration up to the point at which the so-called weak form of the area constraint comes into play.

This work was supported by National Institutes of Health grant AI21002. Computations were conducted using the SGI/Cray Origin 2000 facility of the Boston University Scientific Computing Center.

REFERENCES

- Dembo, M. 1994a. On free boundary problems and amoeboid motion. *In* Biomechanics of Active Movement and Division of Cells. N. Akkas, editor. NATO Advanced Study Institute Series. Springer-Verlag, Berlin. 231–283.
- Dembo, M. 1994b. Solution of a continuum representation of the cytoplasmic mechanics by a finite element method. Los Alamos Unclassified Report no. 94-3454.
- Dong, C., and R. Skalak. 1992. Leukocyte deformability: finite element modeling of large viscoelastic deformation. *J. Theor. Biol.* 158:173–193.
- Dong, C., R. Skalak, and K.-L. P. Sung. 1991. Cytoplasmic rheology of passive neutrophils. *Biorheology.* 28:557–567.
- Dong, C., R. Skalak, K.-L. P. Sung, G. W. Schmid-Schönbein, and S. Chien. 1988. Passive deformation analysis of human leukocytes. *J. Biomech. Eng.* 110:27–36.
- Evans, E. 1984. Structural model of passive granulocyte behavior based on mechanical deformation and recovery after deformation tests. *In* White Cell Mechanics: Basic Science and Clinical Aspects. H. J. Meiselman, M. A. Lichtman, and P. L. LaCelle, editors. Alan R. Liss, New York. 53–71.
- Evans, E., and B. Kukan. 1984. Passive material behavior of granulocytes based on large deformation and recovery after deformation tests. *Blood.* 64:1028–1035.
- Evans, E., and A. Yeung. 1989. Apparent viscosity and cortical tension of blood granulocytes determined by micropipet aspiration. *Biophys. J.* 50:151–160.

- Fletcher, C. A. J. 1984. Computational Galerkin Methods. Springer Series in Computational Physics. Springer-Verlag, New York.
- Frank, R. S., and M. A. Tsai. 1990. The behavior of human neutrophils during flow through capillary pores. *J. Biomech. Eng.* 112:277–282.
- Friedman, G. D., A. L. Klatsky, and A. B. Siegelau. 1974. The leukocyte count as a predictor of myocardial infarction. *N. Engl. J. Med.* 290:1275–1278.
- He, X., and M. Dembo. 1997. On the mechanics of the first cleavage division of the sea urchin egg. *Exp. Cell Res.* 233:252–273.
- Hochmuth, R. M., and D. Needham. 1990. The viscosity of neutrophils and their transit times through small pores. *Biorheology.* 27:817–828.
- Hochmuth, R. M., H. P. Ting-Beall, B. B. Beaty, D. Needham, and R. Tran-Son-Tay. 1993. Viscosity of passive human neutrophils undergoing small deformations. *Biophys. J.* 64:1596–1601.
- Hughes, T. J. R. 1987. The Finite Element Method. Prentice Hall, Englewood Cliffs, NJ.
- Knupp, P., and S. Steinberg. 1994. Fundamentals of Grid Generation. CRC Press, Boca Raton, FL.
- Needham, D., and R. M. Hochmuth. 1990. Rapid flow of passive neutrophils into a 4 μm pipet and measurements of cytoplasmic viscosity. *J. Biomech. Eng.* 112:269–276.
- Needham, D., and R. M. Hochmuth. 1992. A sensitive measure of surface stress in the resting neutrophil. *Biophys. J.* 61:1664–1670.
- Prentice, R. L., T. P. Szatrowski, T. Fujikura, H. Kato, M. W. Mason, and H. H. Hamilton. 1982. Leukocyte counts and coronary heart disease in a Japanese cohort. *Am. J. Epidemiol.* 116:496–509.
- Rash, P. J., and D. L. Williamson. 1990. On shape-preserving interpolation and semi-Lagrangian transport. *SIAM J. Scientific Statist. Computation.* 11:656–687.
- Schmid-Schönbein, G. W., and R. L. Engler. 1986. Granulocytes as active participants in acute myocardial ischemia and infarction. *Am. J. Cardiovasc. Pathol.* 1:15–30.
- Schmid-Schönbein, G. W., K.-L. P. Sung, H. Tözeren, R. Skalak, and S. Chien. 1981. Passive mechanical properties of human leukocytes. *Biophys. J.* 36:243–256.
- Shao, J.-Y., and R. M. Hochmuth. 1997. The resistance to flow of individual human neutrophils in glass capillary tubes with diameters between 4.65 and 7.75 μm . *Microcirculation.* 4:61–74.
- Simon, S. I., and G. W. Schmid-Schönbein. 1988. Biophysical aspects of microsphere engulfment by human neutrophils. *Biophys. J.* 53:163–173.
- Sung, K.-L. P., C. Dong, G. W. Schmid-Schönbein, S. Chien, and R. Skalak. 1988. Leukocyte relaxation properties. *Biophys. J.* 53:331–336.
- Sutton, D. W., and G. W. Schmid-Schönbein. 1992. Elevation of organ resistance due to leukocyte perfusion. *Am. J. Physiol.* 262:H1646–H1650.
- Temam, R. 1979. Navier-Stokes Equations Theory and Numerical Analysis. Studies in Mathematics and Its Applications. North-Holland, Amsterdam.
- Theret, D. P., M. J. Levesque, M. Sato, R. M. Nerem, and L. T. Wheeler. 1988. The application of a homogenous half-space model in the analysis of endothelial cell micropipette measurements. *J. Biomech. Eng.* 110:190–199.
- Ting-Beall, H. P., D. Needham, and R. M. Hochmuth. 1993. Volume and osmotic properties of human neutrophils. *Blood.* 81:2774–2780.
- Tran-Son-Tay, R., D. Needham, A. Yeung, and R. M. Hochmuth. 1991. Time-dependent recovery of passive neutrophils after large deformation. *Biophys. J.* 60:856–866.
- Tran-Son-Tay, R., H. P. Ting-Beall, D. V. Zhelev, and R. M. Hochmuth. 1994. Viscous behavior of leukocytes. In *Cell Mechanics and Cellular Engineering*. V. C. Mow, F. Guilak, R. Tran-Son-Tay, and R. M. Hochmuth, editors. Springer-Verlag, New York. 22–32.
- Tsai, M. A., R. S. Frank, and R. E. Waugh. 1993. Passive mechanical behavior of human neutrophils: power-law fluid. *Biophys. J.* 65:2078–2088.
- Tsai, M. A., R. E. Waugh, and P. C. Keng. 1998. Passive mechanical behavior of human neutrophils: effects of colchicine and paclitaxel. *Biophys. J.* 74:3282–3291.
- Waugh, R. E., and M. A. Tsai. 1994. Shear rate dependence of leukocyte cytoplasmic viscosity. In *Cell Mechanics and Cellular Engineering*. V. C. Mow, F. Guilak, R. Tran-Son-Tay, and R. M. Hochmuth, editors. Springer-Verlag, New York. 33–44.
- Yeung, A., and E. Evans. 1989. Cortical shell-liquid core model for passive flow of liquid-like spherical cells into micropipets. *Biophys. J.* 56:139–149.
- Zhelev, D. V., and R. M. Hochmuth. 1994. Human neutrophils under mechanical stress. In *Cell Mechanics and Cellular Engineering*. V. C. Mow, F. Guilak, R. Tran-Son-Tay, and R. M. Hochmuth, editors. Springer-Verlag, New York. 3–21.
- Zhelev, D. V., and R. M. Hochmuth. 1995. Mechanically stimulated cytoskeleton rearrangement and cortical contraction in human neutrophils. *Biophys. J.* 68:2004–2014.
- Zhelev, D. V., D. Needham, and R. M. Hochmuth. 1994. Role of membrane cortex in neutrophil deformation in small pipets. *Biophys. J.* 67:696–705.